Proposal for an experiment at PSI

Lamb shift in muonic helium

The CREMA collaboration: **C**harge **R**adius **E**xperiment with **M**uonic **A**toms

F. Biraben, P. Indelicato, L. Julien, F. Nez
Laboratoire Kastler Brossel, École Normale Supérieure, CNRS, and Université P. et M. Curie, 75252 Paris, CEDEX 05, France

T.W. Hänsch, T. Nebel, R. Pohl
Max-Planck-Institut für Quantenoptik, 85748 Garching, Germany

J.M.R. Cardoso, L.M.P. Fernandes, A. L. Gouvea, C.M.B. Monteiro, J.M.F. dos Santos
Departamento de Física, Universidade de Coimbra, 3004-516 Coimbra, Portugal

D.S. Covita, J.F.C.A. Veloso
Departamento de Física, Universidade de Aveiro, 3810-193 Aveiro, Portugal

A. Voss, T. Graf
Institut für Strahlwerkzeuge, Universität Stuttgart, 70569 Stuttgart, Germany

K. Schuhmann
Dausinger & Giesen GmbH, 70178 Stuttgart, Germany

A. Antognini, K. Kirch, F. Kottmann, D. Taqqu
Institut für Teilchenphysik, ETH Zürich, 8093 Zürich, Switzerland

M. Hildebrandt
Paul Scherrer Institut, 5232 Villigen-PSI, Switzerland

Y.-W. Liu
Physics Department, National Tsing Hua University, Hsinchu 300, Taiwan

A. Dax
Department of Physics, University of Tokyo, Tokyo 113-0033, Japan

Jan. 20, 2010

Abstract

We propose to measure several transitions frequencies between the $2S$ and the $2P$ states (Lamb shift) in muonic helium ions ($\mu^4\mathrm{He}^+$ and $\mu^3\mathrm{He}^+$) by means of laser spectroscopy, in order to determine the alpha-particle and helion rms charge radius. In addition, the fine and hyperfine structure components will be revealed, and the magnetic moment distribution radius will be determined.

The contribution of the finite size effect to the Lamb shift ($2S-2P$ energy difference) in $\mu\,\mathrm{He}^+$ is as high as 20%. Therefore a measurement of the transition frequencies with a moderate (for laser spectroscopy) precision of 50 ppm (corresponding to 1/20 of the linewidth) will lead to a determination of the nuclear rms charge radii with a relative accuracy of 3×10^{-4} (equivalent to 0.0005 fm). The limiting factor for the extraction of the radii from the Lamb shift measurements is given by the uncertainty of the nuclear polarizability contribution.

Combined with an ongoing experiment at MPQ aiming to measure the $1S-2S$ transition frequency in He^+, the Lamb shift measurement in $\mu\,\mathrm{He}^+$ will lead to a sensitive test of problematic and challenging bound-state QED terms. This measurement will also help to clarify the discrepancy found in our previous μp experiment. Additionally, a precise knowledge of the absolute nuclear radii of the He isotopes and the hyperfine splitting of $\mu^3\mathrm{He}^+$ provide a relevant test of few-nucleon theories.

Contents

1 Beam requirements

Experimental area: πE5.

The proposed experiment needs the same low-energy muon beam as already used for the previous experiment with muonic hydrogen (R98-03). The Cyclotron Trap, the MEC curved magnetic channel, and the PSC/ALC Solenoid have to be installed in the πE5 area in the usual way. The Trap and Solenoid are cryogenic devices which need the usual supply of LHe and LN2.

Required beam properties:

We request negative pions of 106 MeV/c momentum, with maximum momentum bite. The maximum possible beam intensity is needed.

Duration of the experiment:

Most parts of the apparatus are the same as used for the muonic hydrogen experiment in 2009. Some improvements and adaptions will be performed during 2010 and 2011. The status of the Cyclotron Trap is discussed in Sec. 7.2.

The **first beam time** of about 14 weeks is considered for April-July 2012, with the aim to set up the apparatus, search for the first $2S-2P$ resonance line in $\mu\,^4\mathrm{He}^+$, and measure both $\mu\,^4\mathrm{He}^+$ transitions with 50 ppm accuracy.

A second 14-weeks beam time in 2013 will be used to complete data taking for $\mu\,^4\mathrm{He}^+$ and to perform the measurements with $\mu\,^3\mathrm{He}^+$.

Special remarks:

- This experiment uses the PSC/ALC solenoid which is shared with the ALC community. No severe conflicts for the beam time allocation occurred in the past.
- It takes approx. 3 weeks to change the beam line in the πE5 area from the setup used for the MEG experiment to the one needed for our experiment. It is therefore recommendable that our beam time starts immediately after a shut down of the proton accelerator.
- Setting up the whole experiment is a major task, and experience in the past showed that long beam times (at least 14 weeks) are preferable. The laser is permanently installed at a place near the πE5 area but the fine adjustment of the laser beam to the muon target is also non-trivial.
- It is important that the Collaboration knows the beam time allocation at least 6 months in advance, in order to organize the long stays of some members at PSI and to prepare the setup of the apparatus.

2 Questions of safety

(See also page 5, **PSI Declaration List**)

Helium gas will be used and operated at pressure below 1 bar which is not dangerous. The only component which needs careful safety control is the **laser system**. It is the same system as was used in the previous experiment with muonic hydrogen, with some simplifications (no Raman cell is needed). The disk laser emits up to 500 pulses per second with 100 mJ energy per pulse at wavelengths of 1030 nm and 515 nm. The subsequent pulsed Ti:Sa laser emits pulses up to 20 mJ energy at 800-970 nm wavelengths. Suitable protection goggles for the eyes are mandatory.

PAUL SCHERRER INSTITUT – SAFETY SHEET

Ring○ μSR○ SINQ○ Injector1○ SLS○ other○

Declaration List of Hazardous Sample/Target Material and Experimental Equipment
(one form for each item/experiment)

Title of Experiment:	Lamb shift in muonic helium

Experiment Number (if known)	
Instrument / Beamline	PSC device / piE5
Date of Experiment (if known)	from 2011 to 2013

SAMPLE TARGET	name of substance		helium gas
	chemical formula		He
	form of material		powder [ ] liquid [ ] solid [ ] other [x]
	amount of material		1 liter at 4 hPa (=4 mbar)
	size of material		1 liter
	container/sealing:		aluminum vessel
	transport:	by user [ ]	shipped separately [ ] already at PSI [x]
	removed:	by user [x]	stored at PSI [ ] disposed off by PSI [ ]

Toxic	no [x] / yes [ ] , specify:
	ingestion [ ] inhalation [ ] skin contact[ ] eye contact [ ]
	other [ ] , specify:
	contact person: P. Hasler

Already radioactive:	no [x] yes [ ]	activity: Bq	isotopes:	IAEA supervision [ ]
Activation expected:	no [x] yes [ ]	activity: Bq	isotopes:	IAEA supervision [ ]
				contact person: A. Fuchs

Bio. Hazard	no [x] / yes [ ] , specify:
	contact person: K. Ballmer

Reactive:	no [x] / yes [ ] , specify:
	inflammable: [ ] explosive: [ ] corrosive: [ ]
	in contact with: air [ ] water [ ] heat [ ] other:
	contact person: P. Hasler

Equipment during transport/experiment/storage:			contact person	transp.	exp.	storage
magnetic field	5	Tesla	C. Wernli	[ ]	[x]	[ ]
pressure		kbar, m^3	S. Bondt	[ ]	[ ]	[ ]
heating		K, Watt	P. Hasler	[ ]	[ ]	[ ]
cryogenics	4	K, coolant	W. Gloor	[ ]	[x]	[ ]
thin window			L. Simons	[ ]	[ ]	[ ]
X-ray		kV	A. Fuchs	[ ]	[ ]	[ ]
laser	800nm, 0.01 J	λ, W	T. Lippert	[ ]	[x]	[ ]
high voltage	10	kV	M. Huser	[ ]	[x]	[ ]
other:			P. Oggenfuss	[ ]	[ ]	[ ]

Other Safety Aspects:	no [x] / uncertain [ ] / yes [ ], specify
	contact person: P. Oggenfuss

I confirm that the information above is correct as well as to respect all safety regulations valid for PSI.		
Date: 6-Jan-10	E-Mail: franz.kottmann@psi.ch	Signature: F.Kottmann

Please return this form (include attachments if necessary) not later than 3 weeks prior to the experiment to:
W. Bertl (Ring: High Energy), E. Morenzoni (μSR), J. Schefer (SINQ), M. Seidel (Injector 1), C.Schulze (SLS)

3 Introduction and motivation

3.1 Quotes

[http://www.answers.com/topic/rydberg-constant]:
"**Rydberg constant**: The most accurately measured of the fundamental constants[1], which enters into the formulas for wave numbers of atomic spectra and serves as a universal scaling factor for any spectroscopic transition and as an important cornerstone in the determination of other constants; it is equal to

$$R_\infty = \frac{\alpha^2\, m_e\, c}{2\, h} \tag{1}$$

[...] where α is the fine-structure constant, m_e is the electron mass, c is the speed of light, and h is Planck's constant [...]; numerically, it is equal to $R_\infty = 10973731.568527(73)\,\mathrm{m}^{-1}$"

[CODATA 2002, page 75]:
"Advances in the theory of H and D energy levels and an improved value for the proton radius r_p has eliminated the systematic deviation between theory and experiment in the 1998 adjustment and has allowed the task Group to provide recommended values for r_p and r_d. This is a major step forward and increases our confidence in the current formulation of bound-state QED theory."

[CODATA 2002, page 76]:
"In fact, most of these suggestions [for future work] remain valid, because, as for the 1998 adjustment, a key weakness of the 2002 adjustment id the lack of redundancy in the input data. [...] [T]he following needs for new work [...] should resolve key issues and advance our knowledge

- [...]
- *Rydberg constant*:
  One or more measurements of a transition frequency in hydrogen or deuterium with $u_r < 10^{-12}$ [...]
  A measurement of the proton radius with $u_r \approx 10^{-3}$ by means of **spectroscopy in muonic hydrogen** which would also lead to an improved value of R_∞."

[CODATA 2006, page 644]:
"The disagreement of the analytic and numerical calculations [of the B_{60} term in hydrogen, cf. Sec. 13.1.5] results in an uncertainty of the two-photon contribution that is larger than the estimated uncertainty used in the 2002 adjustment. As a result, the uncertainties of the recommended values of the Rydberg constant and proton and deuteron radii are slightly larger in the 2006 adjustment, although the 2002 and 2006 recommended values are consistent with each other."

[CODATA 2006, page 647]:
"An experiment currently underway to measure the Lamb shift in muonic hydrogen may eventually provide a significantly improved value of r_p and hence an improved value of R_∞ (Nebel et al., 2007)"

[CREMA collaboration, to be submitted]:
"This new value of the proton radius is 10 times more precise than the previous one, but it disagrees strongly with the other values: 5σ deviation from CODATA value which is inferred mainly from hydrogen spectroscopy, and 3σ from the value extracted from e-p scattering. The origin of this large discrepancy is not known. [...]
A least-square adjustment of theory and measurements in electronic hydrogen and deuterium as well as in μp results in a Rydberg constant $cR_\infty = 3\,289\,841\,960\,253.9\,(5.1)$ kHz, *i.e.* 107 kHz from the CODATA value [which has an uncertainty of 22 kHz]."

[1] R_∞ has $u_r = 6.6 \times 10^{-12}$. Only the electron g-factor has a smaller uncertainty $u_r = 7.4 \times 10^{-13}$ in CODATA-2006.

3.2 R98-03 "Lamb shift in muonic *hydrogen*"

The present proposal shares much of its collaboration, apparatus and motivation with the recently completed experiment R98-03, "Lamb shift in muonic hydrogen". Therefore we will quickly review the case of muonic hydrogen/deuterium here before we turn our attention to muonic helium.

The main motivations of R98-03 were twofold: On the one hand, the rms charge radius of the proton was considered interesting as a *fundamental property* of the only stable hadron. On the other hand, both calculations of bound-state QED and precision spectroscopy in hydrogen atoms had reached an accuracy where the *test of QED* was limited by the uncertainty of the rms proton charge radius.

The aim of R98-03 was to measure one transition in muonic hydrogen to 30 ppm relative precision and consequently reduce the uncertainty of the proton radius to 0.1% (20 times better than the one from electron scattering), improve the achievable comparison between bound-state QED theory prediction and measurements in the hydrogen $1S$ Lamb shift by an order of magnitude (to 3×10^{-7}), and improve the uncertainty of the Rydberg constant by a factor of six. All these goals have been accomplished in 2009. We measured several transitions in muonic hydrogen and deuterium. This results in improved values for the proton radius, the deuteron radius and the deuteron polarizability. Additionally a Zemach radius value is deduced from the hyperfine splitting in μp with an accuracy comparable to other experiments. Most importantly, however, both transitions in muonic hydrogen show that the proton radius deviates by about 5σ from the previously accepted CODATA value.

3.3 The proton radius discrepancy

Before the μp Lamb shift measurement the proton radius could be determined by two different methods: electron-proton scattering and hydrogen spectroscopy.

- The CODATA [2] value $r_\mathrm{p} = 0.8768(69)$ fm ($u_r = 7.8\times10^{-3}$) is mainly given by **spectroscopy in electronic hydrogen**, assuming that (i) QED is a valid theory, (ii) the QED calculations are mathematically correct, (iii) the QED calculations are complete (no relevant term is missing) and (iv) the measured transition frequencies are correct within their stated errors.
- Sick has reanalyzed the world data on **electron-proton scattering** [3] and gives $r_\mathrm{p} = 0.897(18)$ fm ($u_r = 20\times10^{-3}$). This has so far been the value of r_p relevant for *testing QED* in hydrogen.
- The value we have obtained from **muonic hydrogen** spectroscopy is $r_\mathrm{p} = 0.841(1)$ fm ($u_r = 1.2\times10^{-3}$). This is the most precise value now, but it deviates from the CODATA and Sick values by 5 and 3 of their respective standard deviations [34].

The origin of this discrepancy is still completely unknown. We are confident that theoreticians will soon start to double-check the relevant calculations in both electronic and muonic hydrogen. On the experimental side, several projects are underway which should be able to shed light on the proton radius puzzle and hydrogen spectroscopy:

- Flowers *et al.* of the British National Physics Laboratory have set up an apparatus for a new measurement of the $2S-nS,D$ transitions in electronic hydrogen [6]. This experiment will provide a check of the Paris $2S-8S,D/12S$ measurements [7] who have so far determined the Rydberg constant.
- The $1S-3S$ transition in electronic hydrogen is under investigation both in Paris and in Munich.
- The hydrogen 1S-2S apparatus has been improved in Munich and a new measurement is planned for this spring. Afterward the apparatus is going to be replaced to further increase the accuracy using novel experimental techniques.

- New electron-proton scattering results are expected from the Mainz MAMI/A1 collaboration [8].
- Udem *et al.* are going to measure the $1S-2S$ transition frequency in He^+ [9].

We should also mention that the muonic hydrogen Lamb shift experiment provides a test of low energy QCD theory. Recent lattice QCD, combined with chiral expansion calculations [4], has recently produced a value of $r_p = 0.831(30)$ fm. This is interestingly close to our new μp value.

3.4 Why is μHe^+ interesting?

Apart from the "traditional" approaches summarized above there is now a new road to improve bound-state QED tests. Recent progress in laser technology (a frequency comb at 60 nm [10]) and ion trapping techniques have made it possible to measure the $1S-2S$ transition frequency in hydrogen-like Helium [9]. Such an experiment is well underway now in Garching.

The situation in helium is very much like it was in hydrogen before the success of R98-03:
Testing QED with $He^+(1S-2S)$ requires a precise value of the charge radius of the helium nucleus. Up to now, electron scattering experiments give a value of $r(^4\mathrm{He}) = 1.681 \pm 0.004$ fm ($u_r = 2.5\times10^{-3}$) [11]. A measurement of the Lamb shift in muonic helium ions will ultimately improve the value for the charge radii of ^{3}He and ^{4}He by an order of magnitude, as we show in the next section.

Before, however, we want to summarize the impact of a Lamb shift measurement in $\mu\,He^+$:

- Initially, of course, precise measurements in both electronic and muonic He^+ will help to **resolve the proton size puzzle** by giving a hint, which of the involved theoretical or experimental investigations might be wrong. In particular, a study of both isotopes will provide more detailed tests of the hyperfine structure corrections, including recoil and QED contributions, some of which have not been tested in detail. The real two-body theory that is needed is the subject of many recent work.

Once the puzzle is resolved, the two new measurements will contribute to the test of bound-state QED on the one hand, and to refinement of the Rydberg constant on the other.

- The proposed measurements in $\mu\,He^+$ and He^+ will **test bound-state QED** on a supplementary and more sensitive level than the corresponding hydrogen measurements.

  As elaborated in the theory section below (Sec. 13.2, Table 6), the challenging two-loop QED effects contributing to hydrogen-like atoms scale with $(Z\alpha)^{6...7}$, whereas the Bohr structure scales like $Z^2\,R_\infty$ and the leading finite size effect with $Z^4\,r$, where r is the nuclear radius, α the fine structure constant and Z the nuclear charge. A measurement of the $1S-2S$ transition in He^+ with $u_r = 2\times10^{-14}$ and the $\mu\,He^+$ Lamb shift with 50 ppm, together with an improvement of the theoretical prediction of the polarizability in $\mu\,He^+$ to $u_r = 5\%$ will lead to a test of the interesting QED terms like B_{60} and B_{71} to a level of 50 kHz. This has to be compared with the difference of ~ 400 kHz between the two theoretical predictions: one from an all-order calculation, and the other one based on an expansion/perturbative approach [12].

- Last, **nuclear physics** will benefit from the proposed measurement in $\mu\,He^+$ alone. Precise isotope shift measurements of ^{3}He, ^{6}He, ^{8}He have been accomplished [13] by means of laser spectroscopy, which provide accurate differences of the rms radii relative to ^{4}He. To deduce absolute radii therefore it is necessary to know the absolute radius of the reference isotope ^{4}He. The knowledge of these radii will provide additional useful observables to check theories (NN, NNN, NNNN potentials) of few-nucleon nuclei [14].

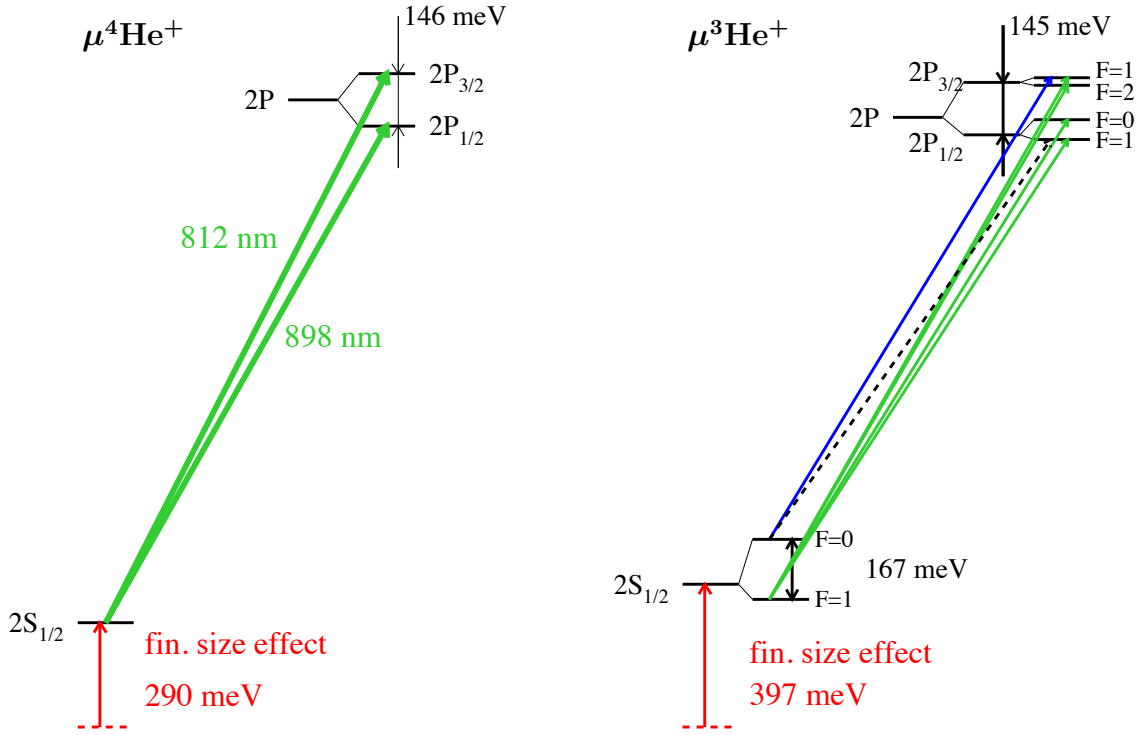

Figure 1: *Level schemes of* $\mu^4\mathrm{He}^+$ *and* $\mu^3\mathrm{He}^+$ *showing the huge finite size effect. The transitions we intend to measure are indicated. In* $\mu^3\mathrm{He}^+$ *we intend to measure all allowed transitions except for the dashed one (cf. Tab. 2) whose wavelength is not accessible to the Ti:Sa laser.*

3.5 Prediction of the $\mu\mathrm{He}^+$ Lamb shift

The Lamb shift in *electronic* H and He is dominated by the electron self-energy, whereas the nuclear effects contribute only on the 10^{-4} level. The muon mass is 200 times the electron mass. This means that in muonic atoms the orbiting particle is moving with an average radius 200 times smaller than in "normal" atoms. As a consequence, the role of electron vacuum polarization corrections, nuclear structure and polarization effects, and recoil contributions dominate. Hence muonic atoms represent a unique laboratory for the determination of nuclear properties. The effect of the finite nuclear size is particularly important for muonic atoms, as can be seen in Fig. 1. The muonic wave function has a significant overlap with the nucleus. The finite size effect is 2% in muonic hydrogen, and 20% in muonic ^{4}He. A comparison of measured Lamb shifts in muonic atoms with the theoretical prediction gives very precise values of the nuclear charge radii (proton, deuteron, ^{3}He, ^{4}He, ...).

The several contributions to the $2P_{1/2} - 2S_{1/2}$ energy splitting in $\mu^4\mathrm{He}^+$ are summarized in Table 1. They are classified as radiative, relativistic, recoil, radiative-recoil, and nuclear structure contributions. QED of a free particle involves only one small parameter, the fine structure constant α. In contrast, bound–state QED needs several expansion parameters: α, $Z\alpha$, m/M, and parameters describing the nuclear structure like the rms charge radius r (see Sec. 13.1.3 for details).

Except for the nuclear polarizability contribution, all corrections to the $\mu^4\mathrm{He}^+$ $2P_{1/2} - 2S_{1/2}$ interval have been calculated with a precision of 0.001 meV [29]. The total predicted splitting is

$$\begin{aligned}
\Delta E(2P_{1/2} - 2S_{1/2}) &= 1670.370(10)(600) - 105.322\, r_{\mathrm{He}}{}^2 + 1.529\, r_{\mathrm{He}}{}^3 \quad \text{meV} && (2)\\
&= 403\,893(2)(145) - 25\,466\, r_{\mathrm{He}}{}^2 + 370\, r_{\mathrm{He}}{}^3 \quad \text{GHz} && (3)\\
&= 1380.020(10)^{\mathrm{th}}(600)^{\mathrm{pol}}(1420)^{\text{fin. size}} \quad \text{meV} && (4)\\
&= 333\,687(2)^{\mathrm{th}}(145)^{\mathrm{pol}}(343)^{\text{fin. size}} \quad \text{GHz} && (5)
\end{aligned}$$

Table 1: *Summary of the* $\Delta E(2P_{1/2}-2S_{1/2})$ *contributions in* $\mu\,^4\mathrm{He}^+$ *from [29]. The leading finite size effect of order* $(Z\alpha)^4$ *and the nuclear structure contribution of order* $(Z\alpha)^5$ *have been adjusted using the most recent alpha-particle radius value of* $r_{^4\mathrm{He}}$*=1.681(4) fm [11]. All terms have been computed with a precision of 0.001 meV.*

Contributions	ΔE (meV)
One-photon VP contribution, $\alpha(Z\alpha)^2$	1665.782
Two-loop VP contributions in first and second order PT, $\alpha^2(Z\alpha)^2$	15.188
Wichmann-Kroll correction	0.135
Three-loop VP in first and second order PT $\alpha^3(Z\alpha)^2$	0.138
Relativistic VP effects	−0.203
Hadronic VP	0.223
μ self-energy, μ VP, μ form factor corrections ($F_1'(0)$, $F_2(0)$)	−11.243
Recoil corrections $(Z\alpha)^4$, $(Z\alpha)^5$, $(Z\alpha)^6$	−0.355
Radiative-recoil corrections	−0.040
Nuclear structure contribution of order $(Z\alpha)^4$: -105.322 $r_{\mathrm{He}}{}^2$	−297.615 (1.420)
Nuclear structure contribution of order $(Z\alpha)^5$: 1.529 $r_{\mathrm{He}}{}^3$	7.261 (0.035)
Nuclear structure and one- two-loop VP+ higher order nucl. structure	−2.357
Nuclear polarizability contribution	3.100 (0.600)
Total splitting	1380.020 meV

where r_{He} is the alpha-particle radius expressed in fermi; $r_{\mathrm{He}} = 1.681(4)$ fm [11] was used. The first uncertainty is related to QED and recoil contributions, the second one is caused by the nuclear polarizability contribution, and the third one is from the finite size effect. The uncertainty related with the finite size contributions is caused not by the pre-factors (-105.322 and 1.529) but by the uncertainty of the radius r_{He} . These uncertainties have to be compared to the 0.069 meV accuracy (corresponding to 50 ppm) we are aiming at.

To conclude, a measurement of $\Delta E(2P_{1/2}-2S_{1/2})$ with 50 ppm precision, combined with the *present* theoretical prediction, will lead to a determination of the ^{4}He radius to a relative accuracy of $u_r = 1\times10^{-3}$. This is a factor 2.5 better as presently known. The limitation in the extraction of the nuclear radius is given by the polarizability contribution.

This polarizability term was calculated in 1976 [33]. It is expected that its uncertainty can be soon reduced at least by a factor of 4, to a 5% relative accuracy [30]. This would lead to a determination of the nuclear radius to $u_r = 3\times10^{-4}$ corresponding to 0.0005 fm.

The theoretical predictions of the 2nd line in $\mu\,^4\mathrm{He}^+$ $(2P_{3/2}-2S_{1/2})$ and the transitions in $\mu\,^3\mathrm{He}^+$ were computed in 1978 [31]. We are confident that updates of these calculations, similar to the 2007 work of [29], will soon be available, once this proposal has been approved.

Our proposed measurement of the Lamb shift in $\mu^4\mathrm{He}^+$ and $\mu^3\mathrm{He}^+$ will ultimately provide the charge radii of both nuclei with ten times better accuracy, *i.e.* **to 0.0005 fm ($u_r = 3\times10^{-4}$).**

4 Experimental principle

The principle of the proposed experiment in $\mu\,\mathrm{He}^+$ is to stop negative muons in He gas whereby highly excited $\mu\,\mathrm{He}^+$ ions are formed. Most of them deexcite quickly to the $1S$-ground state, but $\sim$2% populate the long-lived $2S$-state [15, 16]. A short laser pulse with a wavelength tunable around $\lambda \in [800-970]$ nm (corresponding to ΔE_{2P-2S}) is sent into a mirror cavity surrounding the target gas volume, about $0.9\,\mu$s after the muon stop. $2\mathrm{S} \to 2\mathrm{P}$ transitions are induced on resonance, immediately followed by $2\mathrm{P} \to 1\mathrm{S}$ deexcitation via emission of a 8.2 keV X-ray (lifetime $\tau_{2P} = 0.5$ picoseconds). A resonance curve is obtained by measuring at different laser wavelengths the number of 8.2 keV X-rays which occur in time-coincidence with the laser pulse.

The lifetime of the $\mu\,\mathrm{He}^+$ $2S$-state $\tau_{2\mathrm{S}}$ is crucial for the feasibility of the experiment and its setup. Thus in the following we present a small dedicated section on this topic.

5 $\mu\mathrm{He}^+(2\mathrm{S})$ long-lived population and its lifetime

The lifetime τ_{2S} of $\mu\mathrm{He}^+_{2S}$ states is determined by

$$\tau_{2S}^{-1} = \tau_{\mu}^{-1} + \lambda_{xx} + \lambda_Q, \tag{6}$$

where $\tau_\mu = 2.2\,\mu$s is the muon lifetime and $\lambda_{xx} = 1.18 \times 10^5$ s^{-1} [17] is the $2S-1S$ two-photon decay rate. The quenching rate λ_Q results from collisions with neighboring atoms and thus depends on the He pressure p_{He}.

Experimentally it was found [15, 16] that λ_Q is the sum of a linear and a quadratic term in the He pressure p_{He}:

$$\lambda_Q = k_1\, p_{\mathrm{He}} + k_2\, p_{\mathrm{He}}^2. \tag{7}$$

For $T = 293$ K it was measured that

$$\begin{aligned} k_1 &= (2.7 \pm 1.0) \times 10^3 \quad [\mathrm{hPa}^{-1}\,\mathrm{s}^{-1}] \\ k_2 &= (37 \pm 4) \qquad\qquad\quad [\mathrm{hPa}^{-2}\,\mathrm{s}^{-1}]\,. \end{aligned}$$

The linear term dominates at pressures below 70 hPa. It is leading to emission of 8.2 keV X-rays. Such "collisional quenching" occurs during a collision with a He atom. The quadratic term is relevant at higher pressures. It corresponds to the formation of molecular ions He-$\mu\mathrm{He}^+_{2S}$ in three-body collisions, with subsequent deexcitation to the μHe ground state within a few ns. About half of these molecules deexcite non-radiatively via Auger-decay.

The resulting $2S$-lifetimes are, *e.g.*, 1.75 μs in vacuum, 1.71 μs at $p_{\mathrm{He}} = 4$ hPa, and 1.35 μs at $p_{\mathrm{He}} = 40$ hPa. At 4 hPa where we plan to perform the Lamb shift experiment there will be an emission of delayed 8-keV X-rays at a rate of 1.1×10^4 s^{-1} which contributes to the background at delayed times (see Sec. 8).

In the 1970s the $2S-2P$ energy difference in $\mu^4\mathrm{He}^+$ ions was measured at CERN at a He pressure of 40 **bar** [18, 19]. This experiment relied on a sufficiently long $2S$-lifetime ($\sim 1\,\mu$s) and a relative $2S$-population of a few percent. Such long lifetimes were in contradiction with theoretical predictions about collisional $2S$-quenching. The $2S$-lifetime was therefore investigated by three independent groups in the 1980s [15, 20, 21], and all of them found very short $2S$-lifetimes at pressures above 1 bar.

Based on these facts a laser experiment was performed at SIN (now PSI) with the aim to find the $2S-2P$ resonance in $\mu\,^4\mathrm{He}^+$. It was shown that this resonance line is certainly not at the position predicted by the old CERN experiment [22]. Unfortunately the event rate was too low to perform a

search for the resonance transition at various laser wavelengths. The experiment was not rebuilt after the 1990/1 reconstruction of the PSI experimental hall.

Another important parameter for the laser experiment is the relative $2S$-population ε_{2S}. It can be deduced from the measured K-line yields which depend on pressure [15, 16]. The values are, *e.g.*, $\varepsilon_{2S} = 2.3 \pm 0.3$ % at 8 hPa, and $\varepsilon_{2S} = 2.6 \pm 0.3$ % at 40 hPa. An extrapolation gives a long-lived 2S population of

$$\varepsilon_{2S} = 2.2 \pm 0.3 \text{ \% at 4 hPa.} \tag{8}$$

6 μHe$^+$ transitions: wavelengths, probabilities and laser intensities

In this section we present the most important parameters of all the possible one-photon transitions between the $2S$ and the $2P$ state in $\mu\,\mathrm{He}^+$. These parameters are the transition frequency (wavelength), the transition probability (which depends on the transition matrix element), the laser energy required to saturate the transition, the relative population of the initial states and the linewidths.

If a $\mu\,\mathrm{He}^+$ ion in the $2S$ state is subject to an intense pulse of radiation of suitable frequency, a transition to the $2P$ state can be induced. This transition is immediately followed by a spontaneous emission of an 8.2 keV photon bringing the $\mu\,\mathrm{He}^+$ ion into the $1S$ ground state. This 8.2 keV photon will be used as a signature of the $2S-2P$ transition. The transition rate $\lambda_{a,b}$ from state a to state b is given by Fermi's Golden Rule

$$\lambda_{a,b} = \frac{2\pi}{\hbar^2} \,|<b|H_{\mathrm{int}}|a>|^2 \, \frac{\Gamma/2\pi}{(\omega-\omega_0)^2+\Gamma^2/4} \tag{9}$$

where $\Gamma = \Gamma_a + \Gamma_b$ is the transition linewidth (sum of initial and final state decay rates), ω the laser frequency, ω_0 the transition frequency and $|<b|H_{\mathrm{int}}|a>|$ is the transition matrix element. The Hamilton operator describing the interaction of light with the atom in the electric dipole approximation is given by $H_{\mathrm{int}} = \frac{e}{mc}\vec{A}\cdot\vec{p}$, where $\vec{A}$ is the laser field vector potential, $\vec{p}$ the muon momentum and m the reduced mass of the system. In the dipole approximation we find that

$$|<b|H_{\mathrm{int}}|a>|^2 = 2\pi\hbar\alpha\, I \,|<b|\vec{\epsilon}\cdot\vec{r}|a>|^2 \tag{10}$$

where I is the laser intensity [W/cm^2]. The calculation of these matrix elements involves an integration over a radial part ($R_{nl}^{n'l'}$), integration over an angular component which can be calculated with Clebsch-Gordan coefficients, an average over the dipole moment relative to the polarizations ($\vec{\epsilon}$) of the light field, an average over initial spin projection and a sum over final spin-projection states. For the simple case of $\mu\,^4\mathrm{He}^+$ we have

$$|<2P_{1/2}|\vec{\epsilon}\cdot\vec{r}|2S_{1/2}>|^2 = \frac{1}{3}(R_{20}^{21})^2 \equiv f_{1/2,1/2}(R_{20}^{21})^2 \tag{11}$$

$$|<2P_{3/2}|\vec{\epsilon}\cdot\vec{r}|2S_{1/2}>|^2 = \frac{2}{3}(R_{20}^{21})^2 \equiv f_{1/2,3/2}(R_{20}^{21})^2 \tag{12}$$

where $R_{20}^{21} = -3\frac{a_\mu}{Z}$ with a_μ being the muonic Bohr radius. Table 2 reports the f coefficients for all transitions.

On resonance ($\omega = \omega_0$) the transition probability is given by

$$\lambda_{a,b} = k \cdot f_{a,b} \cdot I \tag{13}$$

where the constant k is

$$k = \frac{72\pi\alpha}{\hbar}\cdot\left(\frac{a_\mu}{Z}\right)^2\cdot\frac{1}{\Gamma} = \begin{cases} 1.36\ [\frac{\mathrm{cm}^2}{\mathrm{J}}] & \text{for } \mu\,^4\mathrm{He}^+ \\ 1.40\ [\frac{\mathrm{cm}^2}{\mathrm{J}}] & \text{for } \mu\,^3\mathrm{He}^+ \ . \end{cases} \tag{14}$$

Since a_μ is inversely proportional to the reduced mass m, $a_\mu \sim 1/m$, and $\Gamma \sim Z^4\, m$ we see that k scales like $k \sim m^{-3} Z^{-6}$. Because of the m^{-3} dependence the laser intensity need to be 10^7 higher than an equivalent transition in normal atoms and around 2^6 times higher than the equivalent transition in μp. Luckily our laser system (cf. Sec. 7.4) will be operated without the Raman cell, so we will win a factor of ~ 60 in laser pulse energy.

The excitation probability for $\Gamma_{2P} \gg \lambda_{a,b}$ is governed by following differential equation:

$$\frac{dw_{a,b}(t)}{dt} = \lambda_{a,b}(1 - w_{a,b}(t)) \tag{15}$$

$$w_{a,b}(0) = 0 \qquad \text{initial condition}\,. \tag{16}$$

The general solution for a laser pulse with intensity $I(\omega, t)$ and duration $T \ll \tau_{2S}$ takes the form

$$w_{a,b}(T) = e^{-\Lambda_{a,b}(T)} \cdot \int_0^T \lambda_{a,b}(t) \cdot e^{\Lambda_{a,b}(t)}\, dt \tag{17}$$

$$\Lambda_{a,b}(T) = \int_0^T \lambda_{a,b}(t)\, dt\,. \tag{18}$$

On resonance it simplifies to:

$$w_{a,b}(\omega_0) = 1 - e^{-f_{a,b} \cdot k \cdot F(\omega_0)} \tag{19}$$

$$F(\omega_0) = \int_0^T I(\omega_0, t)\, dt = \frac{E_{\text{laser}}}{A} \equiv \text{Fluence}\,. \tag{20}$$

We can define the **saturation fluence** to be $F_{\text{sat}} = \frac{1}{f_{a,b} \cdot k}$ so that the transition probability on resonance simplifies to:

$$w_{a,b} = 1 - e^{-F/F_{\text{sat}}}. \tag{21}$$

The saturation fluence F_{sat} for the various transitions is given in Tab. 2. For small fluences ($f_{a,b}\, k\, F(\omega_0) \ll 1$) we can linearize this equation to $w_{a,b} = F/F_{\text{sat}}$.

The $2S - 2P$ transition rate W is given by

$$W = \eta \cdot \varepsilon_{2S} \cdot (1 - e^{-F/F_{\text{sat}}}) \tag{22}$$

where $\varepsilon_{2S} = 2.2 \pm 0.3$ % is the $2S$ population at 4 hPa target gas pressure (cf. Sec. 5), and η is the sub-level population as listed in Tab. 2. We see that the event rate is linearly proportional to the initial sub-level population. For transitions with small matrix elements one can increase the transition probability (and henceforth the event rate) only by increasing the laser pulse energy.

On resonance, the saturation fluence transfers 63 % of the $2S$ population into the $2P$ state. At the same time there is power broadening

$$\text{FWHM} = \Gamma \left(1 + \frac{F}{F_{\text{sat}}}\right)^{1/2} \tag{23}$$

due to the fact that the transition probability saturates at the peak of the resonance line, whereas it is still linear in the wings. To avoid line broadening we will perform the measurements at fluences $\leq 1/2\ F_{\text{sat}}$, so we will transfer at most 30% of the sublevel population.

As we will see in Sec 7.4.5, a pulse of 10 mJ energy from the Ti:Sa laser causes a laser fluence of 1.4 J/cm^2 in the cavity surrounding the muon stopping volume. We will therefore reduce the laser pulse energy for transitions with saturation fluence < 2.8 J/cm^2, keeping the $2S - 2P$ transition probability at $\sim 30\%$ to avoid power broadening. The expected signal rates in Tab. 2 have been

calculated accordingly. Saturation fluences larger than 2.8 J/cm^2 cause a decrease of the event rate as can be seen from the Table.

Finally we have to consider the transition wavelengths accessible with our Ti:sapphire (Ti:Sa) laser. The maximum of the Ti:Sa laser gain is at 795 nm, and we can drive all but the 1108 nm transition in μ^3He$^+$ with our Ti:Sa laser. The given rate estimates also account for the reduction of the available laser energy when operating the laser at wavelengths > 900 nm.

Accounting for these facts we plan to measure the several transitions in two successive phases (beam times): In **phase 1** we intend to measure both transitions in μ^4He$^+$. The gas handling of ^{3}He needs special attention, so we plan to measure several transitions in μ^3He$^+$ during **phase 2**, one year after μ^4He$^+$ has been measured.

The goal of the experiment is to measure each of the accessible transition frequencies with an accuracy of 50 ppm. The centroid position must thus be determined with an accuracy of approximately 20 GHz, which corresponds to $\sim \Gamma/20$. The natural linewidth $\Gamma = 320$ GHz (corresponding to 0.9 nm) is huge. It is about 10^{-3} of the total $2S-2P$ energy difference! From the statistics point of view, 500 events in the resonance are sufficient to be able to reach such goal (see Sec. 8).

Table 2: $2S-2P$ *transition properties for* μ^4He$^+$ *and* μ^3He$^+$. *We give energy difference, wavelength, sub-level population* η*, transition matrix element, transition strength* $f_{a,b}$*, laser fluence required to saturate the transition* $F_{\rm sat}$*, and expected event rate (cf. Sec. 8). The event rates have been calculated assuming a (constant) 30% transition probability for saturation fluences up to 2.8 J/cm*^{2} *(to avoid power broadening of the resonance line the laser energy has to be adapted when possible). Additionally the event rates account for the expected decrease of the laser energy with increasing wavelength. The transition at 1108 nm cannot be accessed with a Ti:sapphire laser. The energy differences and wavelengths for the* μ^4He$^+$ *transitions have been taken from [29] and adjusted to the most recent value of the nuclear radius* $r_{^4He} = 1.681\,(4)$ *fm [11]. The* μ^3He$^+$ *transitions energies have been taken from [32] and adjusted to a* ^{3}He *nuclear value of* $r_{^3He} = 1.971\,(4)$ *fm (deduced from* $r_{^4He}$ *and the recent measurement of the isotope shift [13]).*

Isotope	Transition	ΔE [meV]	λ [nm]	Pop.(η)	Mat. el. [a_μ]	$f_{a,b}$	$F_{\rm sat}$ [J/cm^2]	event rate [h^{-1}]
μ^4He$^+$	$2S_{1/2} - 2P_{3/2}$	1526	812	1	6	8/12	1.1	48
μ^4He$^+$	$2S_{1/2} - 2P_{1/2}$	1380	898	1	3	4/12	2.2	48
μ^3He$^+$	$2S^{F=0}_{1/2} - 2P^{F=1}_{1/2}$	1119	1108	1/4	3	1/12	2.1	—
μ^3He$^+$	$2S^{F=0}_{1/2} - 2P^{F=1}_{3/2}$	1294	958	1/4	6	2/12	1.1	12
μ^3He$^+$	$2S^{F=1}_{1/2} - 2P^{F=1}_{1/2}$	1286	964	3/4	2	2/12	3.2	22
μ^3He$^+$	$2S^{F=1}_{1/2} - 2P^{F=0}_{1/2}$	1344	923	3/4	1	1/12	6.4	13
μ^3He$^+$	$2S^{F=1}_{1/2} - 2P^{F=2}_{3/2}$	1436	863	3/4	5	5/12	1.3	36
μ^3He$^+$	$2S^{F=1}_{1/2} - 2P^{F=1}_{3/2}$	1461	849	3/4	1	1/12	6.4	16

7 Apparatus

In this section we discuss our experimental setup of muon beam line, laser system, detector-target-assembly and DAQ system. **We need basically the same setup we used in the 2009 beam time of the μp experiment.** Only few changes have to be applied to the existing setup. The major ones are:

- Removal of the Raman cell since we need laser pulses in the wavelength region $\lambda \in [800 - 970]$ nm (depending on the chosen transition)
- New LAAPDs optimized to detect 8.2 keV instead of 1.9 keV as for the μp experiment.

The removal of the Raman cell represents a major simplification of the present laser system, and the detection of the 8.2 keV single photons is simpler than detecting X-rays at 1.9 keV. Following the detailed description of all the setup components, at the end of this section, we will stress what are the major changes, what will be the simplifications and the needed work.

7.1 Muon beam line, target and X-ray detectors

The $\mu\,\mathrm{He}^+$ Lamb shift experiment will be performed at the PSI πE5 beam-line. For the μp experiment R98-03 we have built a beam line for low-energy muons ($\sim 5\,\mathrm{keV}$ kinetic energy), which yields an order of magnitude more muon stops in a small low-density gas volume than a conventional muon beam.

Our muon beam (Fig. 2) consists of the *Cyclotron Trap* (CT) for the production of low energy muons, the *muon extraction channel* (MEC) which is a curved solenoid for the transport and the selection of these muons, and the 1 m long *PSC* solenoid containing the gas target and two transmission detectors for the muons.

$10^8\,\mathrm{sec}^{-1}$ negative pions with a momentum of $102\,\mathrm{MeV/c}$ enter the cyclotron trap (CT) tangentially, where they are moderated by passing a degrader. About 30 % of the pions decay into μ^- which are further decelerated by repeatedly passing a metalized thin Formvar foil. The two superconducting magnetic ring-coils of the CT act as a magnetic bottle confining the μ^-. The μ^- slow down until the repulsive electric field/potential applied to the moderator foil dominates over the magnetic forces.

Muons escaping the CT enter the MEC, a toroidal momentum filter assembled from normal conducting magnetic coils (magnetic field $B = 0.15\,\mathrm{T}$). It favors muons with $\sim 20\,\mathrm{keV}$ energy and separates them from unwanted background radiation and particles. From the MEC, the muons are guided into the bore hole of a 5 Tesla superconducting PSC magnet, slightly above its axis.

The schematic view of the setup inside the PSC solenoid is shown in Fig. 3. The solenoid's high magnetic field ensures minimal radial size of the muon beam thereby reducing the target volume to be illuminated by the laser. Before entering the He target, the muons pass two stacks (S_1 and S_2) of ultra-thin carbon foils ($d = 4\,\mu\mathrm{g/cm}^2$ for each foil) kept at high electric potential which both serve as muon detectors and decelerate the muons to 5–8 keV. Each muon releases a few electrons in the stack-foils which are separated from the much slower muons in an $\vec{E} \times \vec{B}$ separator field. The electrons are detected by plastic scintillators and photomultiplier tubes and provide the trigger signal for the data acquisition system and the laser. The trigger signal results from the coincidence (with the TOF for 5 keV muons) between the electrons from S_1 (detected in the photo multiplier PM_1) and S_2 (seen in PM_2 or PM_3).

The number of detected muons is 330 s^{-1} at a proton beam current of $1900\,\mu\mathrm{A}$. The S_1 and S_2 detector efficiencies are 80% and 70% (resulting from 55% downstream, 35% upstream photomultiplier detector) respectively. The trigger quality, *i.e.* the fraction of stopped muons to detected muons, is $Q \approx 60\%$ at 4 mbar.

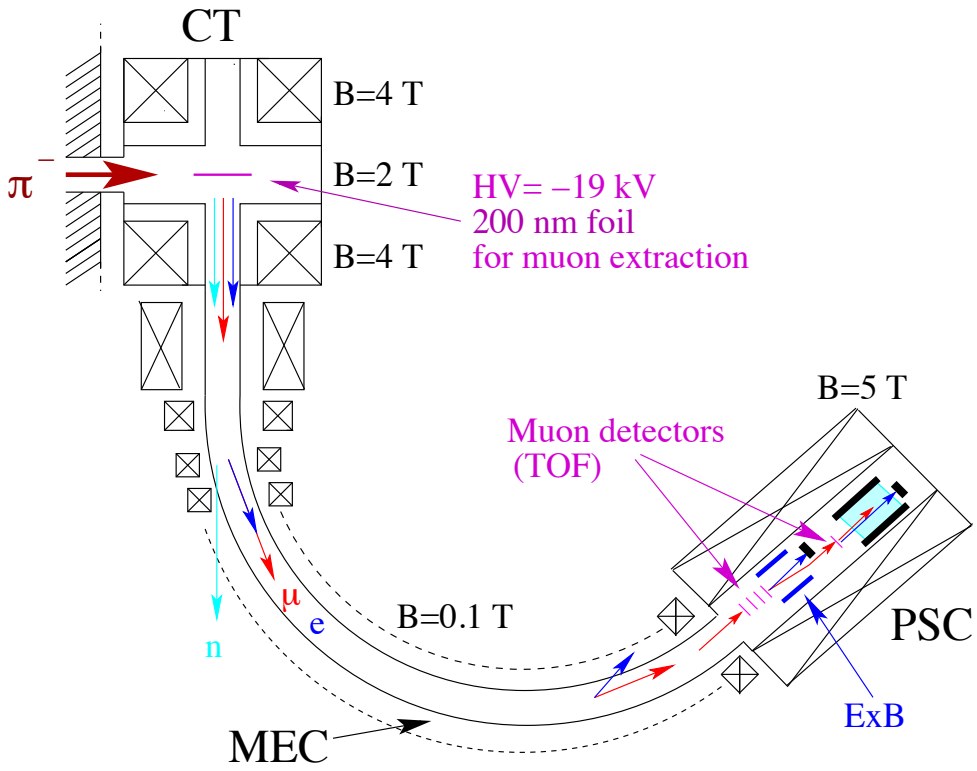

Figure 2: *Layout of the πE5 area with Cyclotron Trap, muon extraction channel MEC, and PSC solenoid ($B = 5$ T). Details of the setup inside the solenoid are shown in Fig. 3.*

Finally, the muons arrive in the gas target volume which is filled with 4 hPa of He gas and, along the beam axis, has a length of 20 cm. The transverse dimensions of the stop volume are $5\times12\,\mathrm{mm}^2$. Above and below, two face-to-face arrays of Large Area Avalanche Photo–Diodes (LAAPDs) record the 8.2 keV K_α X-rays in a distance of 8 mm from the muon beam axis. The LAAPDs signals are amplified and stored in an 12-bit waveform digitizer operated at 250 MHz. This allows an optimal suppression of background signals with non–standard shape and the separation of two consecutive superimposed pulses in the analysis. For the μp experiment we have used beveled LAAPDs from *Radiation Monitoring Devices (RMD)* to detect the 1.9 keV X-rays. The minimum detectable energy was 1 keV, the average resolution at 1.9 keV was 25%, and (FWHM) $\Delta t \approx 40$ ns when the LAAPDs were cooled at -30° [23, 24]. We have measured that the efficiency of these LAAPDs at 8 keV is approximately a factor of 2 smaller than at 2 keV, and that the maximum is reached at 3.5 keV [26]. Obviously, although this decrease of efficiency does not affect the feasibility of our experiment (see event rate estimations) we will put effort to test other type of LAAPDs which have a larger efficiency in the 8 keV region.

The muon beam line will not be changed between 2009 and the next beam time. The target pressure will increase from 1 mbar of H_2 (2009) to 4 mbar of He. This will be advantageous resulting in a better muon stop distribution and muon stopping rate (×1.5) because of the increased trigger quality Q: At higher pressure, more muons stop in the fiducial volume of the target.

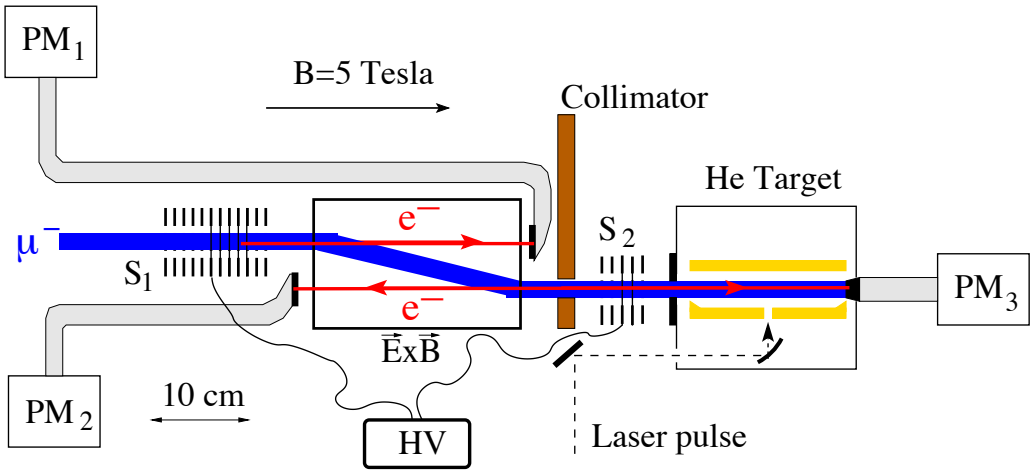

Figure 3: *Schematic view of the apparatus mounted inside the 5 T solenoid. The muons enter from the left and cross two stacks of ultra–thin carbon foils, S_1 and S_2, which act together with PM_1, PM_2 and PM_3 as two muon detectors. The $\vec{E} \times \vec{B}$ filter (shown in side view) separates μ^- from e^-. The gas target is filled with 4 hPa He gas and it is separated by the vacuum of the muon beam line by a 30 nm thick Formvar foil. The laser cavity mirrors (shown in top view) are placed sideways of the muon stop volume. The laser light enters the vacuum vessel and the gas target and reaches the multipass mirror cavity (shown in yellow) through a hole in one of the cavity mirror. Two LAAPD arrays are mounted above and below the muon stop volume (not shown in the picture).*

7.2 Cyclotron Trap

The Cyclotron Trap is the first stage of the low-energy muon beam. It has been operated successfully for many years. There were problems in the 2009-beam time because there was a short-circuit of one of the two coils, which obviously touched the inner surface of the assembly. This problem occurred after a sequence of cooling down and heating up of the cryogenic part which was not the usual one. The problem was solved after we heated up the whole assembly to room temperature and cooled it down again, following the usual procedure.

We therefore expect that this problem will not occur in future. In principle a repair of the Trap is possible, as was done several years ago by Marti Company together with PSI workshop and other PSI groups, but this would be a work of several months and considerable costs (of order 50 kCHF), and the risk of failure cannot be totally excluded. (Oxford Company, the original supplier, is not anymore capable to do it.)

It is foreseen that the Cyclotron Trap will be transported to Paris University (Laboratoire Kastler Brossel) in May 2010 and back to PSI in Nov. 2011. Paul Indelicato (one of our collaborators) will use it as part of an ECR ion source developed at PSI by Leo Simons et al.

Depending on the experience that we gain during operation at Paris, we will decide about the future of the Trap.

In principle, the μHe Lamb shift experiment proposed here could be performed also at the πE5 beam line operated in the "cloud muon" mode, using a very low momentum of 10 MeV/c. We got experience with this mode in the mid-1990s when we successfully stopped negative muons in hydrogen gas at pressures between 64 hPa and 0.06 hPa (measurement of the kinetic energies of μp atoms). To use this beam would however need considerable changes of the muon entrance detectors and the laser beam line.

7.3 LAAPDs: Detectors for 8.2 keV X-rays

The μHe experiment requires X-ray detectors which work in a magnetic field of 5 Tesla, which are relatively compact, and have a large area, good energy resolution, and fast time response.

Large area APDs (LAAPDs) from RMD *(Radiation Monitoring Devices, Inc.)* with an active area of 14x14 mm^2, operated at -30 °C, were used in the previous μp experiment. Typical energy and time resolutions for the muonic hydrogen K_α X-rays at 1.9 keV were 25 % (FWHM) and 40 ns. Two rows of 10 such APDs were mounted above and below the target cell. These APDs did not show any degradation of performance in the 5 Tesla magnetic field of our solenoid.

The RMD APDs are optimum for the detection of 1.9 keV X-rays from μp ($\sim$ 80 % detection efficiency) but not for the 8.2 keV muonic helium K_α X-rays. There the efficiency drops to $\sim$ 40 % because the depletion region is relatively thin ($\sim 30\,\mu$m).

We will investigate, together with RMD, the possibility to produce APDs with thicker depletion regions.

Recently, Hamamatsu Photonics has developed APDs of the *"reach-through"* type with thicker depletion layer ($\sim 130\,\mu$m) which makes them suitable for detecting X-rays up to 20 keV [60]. For 8 keV X-rays their detection efficiency is above 90 %. APDs of this type, with 3 mm diameter, have demonstrated a good energy resolution of 6.4 % for 5.9 keV X-rays and an excellent time response of a few ns [60]. Prototypes with larger area may be produced by the company, increasing the solid angle for X-ray detection.

Another possibility to obtain a good efficiency at 8 keV would be to glue a thin scintillator plate (*e.g.*, LYSO) onto an APD (of the type we already have). The amount of scintillation light produced by an 8 keV X-ray will give a signal in the APD whose amplitude is of the same order as produced by a 2 keV X-ray without scintillator. The efficiency would be $\sim$ 90 % in this case, the timing reasonably fast (depending on the scintillator properties), but the energy resolution relatively poor.

The collaboration will perform a research and development program in 2010 and 2011 in order to find the optimum solution for the X-ray detector. In any case, the existing LAAPDs from RMD can still be used, reducing the quoted event rates only by a factor of 2. (This is then still a 4 times larger event rate than in the μp run 2009).

7.4 Laser system

7.4.1 The muonic *hydrogen* laser system

The design of the laser as it exists in the laser hut close to the πE5 area has historically been dictated by the need for tunable 6 μm light output within 1 μs after a random trigger. The lifetime of the $2P$ state in muonic *hydrogen* is 1 μs. The $2S$ lifetime in $\mu\,\mathrm{He}^+$ is 1.7 μs, so the laser is fast enough.

In addition, the Ti:sapphire laser has been optimized to deliver 5 ns short pulses suitable for optimal conversion in the multipass Raman cell. This resulted in a rather short Ti:sapphire oscillator cavity, followed by a multipass Ti:sapphire amplifier delivering 15 mJ of red light at $\lambda \in [700 - 710]$ nm.

For the $\mu\,\mathrm{He}^+$ experiment the Ti:sapphire light will be used directly. This has several advantages:

- The Ti:sapphire oscillator can be made longer resulting in longer output pulses (*e.g.*, 50 ns). This reduces the laser damage threshold problems of the optical components significantly.
- The Raman cell converted 15 mJ of red light into 0.25 mJ of IR light for the spectroscopy in muonic hydrogen. We will now avoid this loss of 98% of the available pulse energy.
- The light traveled 35 times 2 m = 70 m inside the Raman cell resulting in 230 ns laser delay. This can be avoided now, too.

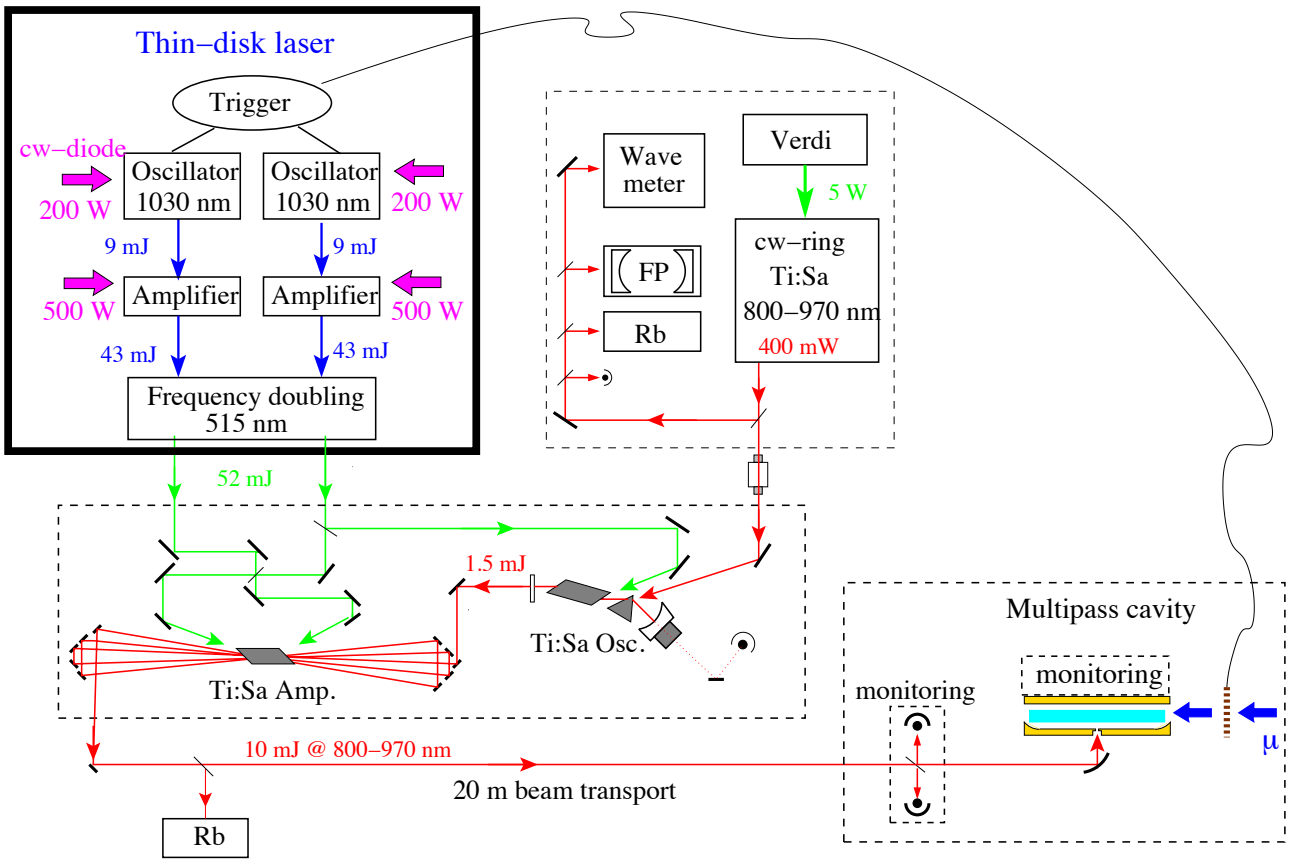

Figure 4: *Schematic view of the laser system. The main components are a pulsed thin-disk laser with frequency doubling, a tunable cw Ti:Sa laser, a pulsed oscillator–amplifier Ti:Sa laser, and a multipass mirror cavity with its diagnostic system. FP: Fabry–Perot, Rb: Rubidium absorption cell.*

- Alignment of the Raman cell was rather subtle and time-consuming.
- The light leaving the Raman cell was easily absorbed by humidity in air and care had to be taken to guide the light to the πE5 area through a vacuum system. This is not the case for the visible light required for $\mu\,\mathrm{He}^+$ spectroscopy.

7.4.2 Laser requirements for $\mu\mathrm{He}^+$

The laser system has to deliver pulses of 10 mJ at 812 nm[2], has to be stochastically triggerable, with average rates $\simeq 500\ \mathrm{s}^{-1}$ and with a delay between trigger to arrival of the pulse inside the cavity $< 1.7\ \mu$s. The laser has to be tunable for 2 THz (5 nm) around each predicted transition frequency, and it has to have a bandwidth < 10 GHz to search and scan for the resonance.

The laser system (see Fig. 4) is composed of a pulsed thin-disk laser [28] and a pulsed oscillator-amplifier Titanium-Sapphire (Ti:Sa) laser whose frequency is injection-seeded (that is, controlled) by a continuous (cw) Ti:Sa laser [27]. The laser pulses produced by the Ti:Sa laser at 812 nm are then transported into the zone via our existing laser beam transport tube, and coupled to a multipass enhancement cavity, illuminating the muon stopping volume. This system is very similar with the one used in the μp experiment besides

[2]In this section, for simplicity, we give the numbers required for the measurement of the first transition in $\mu\,\mathrm{He}^+$, *i.e.* the transition at 812 nm. The different matrix elements and wavelengths ($\lambda \in [800 - 970]$ nm) of the other transitions have been taken into account in the transition rate estimates.

- *removal of the Raman cell:* see Sec. 7.4.1
- *different wavelength ($\lambda \in [800 - 970]$ nm):* This is easily accomplished by replacing the optical components (mirrors, fibers, beam splitters etc.) In particular, the departure from the 6 μm wavelength region simplifies tremendously the availability of mirrors, detectors, and in particular the target cavity coatings.

We can already conclude at this point that the present laser system with small adjustments (because of the different Ti:Sa wavelength) will fulfill all the requirements.

7.4.3 Disk laser

The muon entrance detectors trigger two parallel Yb:YAG thin-disk laser systems. Each disk laser system is a Q-switched oscillator followed by a 12-pass amplifier [28]. A fiber coupled diode laser continuously pumps the thin-disk laser with 1.2 kW of radiation at 940 nm, so that the energy is continuously stored in the disk active material (upper level lifetime ~ 1 ms). To achieve a minimal intrinsic delay of the laser pulse buildup we operate the Yb:YAG oscillators in "cw-prelasing" mode.

After a muon-trigger, the Q-switched oscillator cavities are closed by switching one of the two HV-electrodes of their Pockels cells (PC) within a few nanoseconds. Fast intra-cavity pulse build-up follows.

About 200 ns later the cavities are opened by switching the second electrode of the PC. The circulating power is thus released. Each oscillator delivers a 9 mJ pulse at 1030 nm with a beam-quality factor $M^2 < 1.1$ and an delay of only 250 ns after the muon trigger.

The two thin-disk amplifiers boost each pulse to 43 mJ using a novel configuration whose main peculiarity is its insensitivity to thermal lens effects even for large beam waists [28].

A frequency doubling stage based on LBO crystals is used to convert the two disk-laser pulses from 1030 nm to 515 nm which is a suitable wavelength for the pumping of the Ti:Sa laser. We achieved a stable output of 27 mJ at 515 nm per system during the run 2009.

7.4.4 Ti:Sa laser

The Ti:Sa laser is a concatenation a wavelength-selective master-oscillator cavity and a bow-tie configuration multi-pass power-amplifier. It is pumped with a total of 54 mJ at 515 nm wavelength, and lases at 812 nm. The 1.5 mJ pulses emitted from the oscillator are boosted in the amplifier to 15 mJ. The frequency of the Ti:Sa laser is controlled by injection seeding the Ti:Sa oscillator with a single-mode cw-Ti:Sa laser. Tuning the wavelength of the cw Ti:Sa laser therefore leads to a tuning of the frequency of the Ti:Sa pulses.

The stability of the cw Ti:Sa laser is guaranteed by locking it to an external reference Fabry-Perot cavity. This temperature stabilized and low expansion Fabry-Perot cavity was calibrated by means of two-photon spectroscopy of well-known Rb and Cs lines. The resulting free spectral range was measured to be 1497.33(4) MHz in the 812 nm region. The frequency of the cw Ti:Sa laser is thus absolutely known with a precision of 30 MHz.

The frequency of the pulsed Ti:Sa laser equals the frequency of the cw one, apart from a frequency chirp we have measured to be of the order of 200 MHz. In order to avoid uncertainties related with any chirping effects in the Ti:Sa laser we do not only calibrate the cw-Ti:Sa laser but also the pulses by means of Cs one- and two-photon spectroscopy. In such a way the frequency of the pulse we use to drive the $2S - 2P$ resonance is known over all scanning range with an accuracy better than 200 MHz. This uncertainty is negligible with the expected statistical error of 20 GHz.

7.4.5 Multipass cavity

The 812 nm laser pulse is then coupled into a (non-resonant) multipass cavity surrounding the muon stop volume. The cavity is shown in Fig. 5. It follows the design of the μp cavities. Here, we had also some training cavities for visible laser light (6 μm light is very hard to play with.)

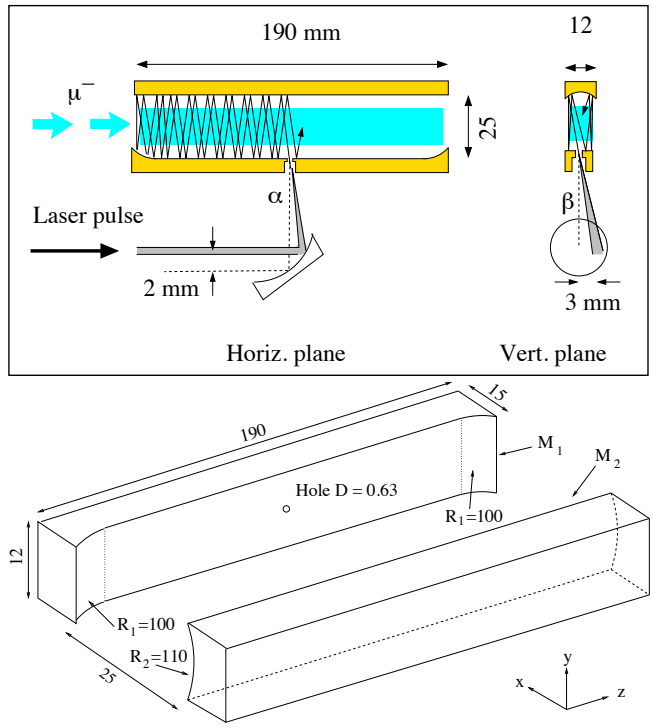

Figure 5: *Impression of the multi–pass mirror cavity. Curvatures are greatly exaggerated. Dimensions are given in mm.*

The cavity is designed to be very insensitive to misalignment and to illuminate a large volume reasonably homogeneously. The cavity's design is so robust that we can avoid any active stabilization.

The laser pulse enters the cavity via a 0.6 mm diameter hole in one of the mirrors. The cylindrical mirror M_2 confines the light in the vertical direction, whereas the two cylindrical pieces attached to the flat mirror M_1 guarantee the confinement in the horizontal direction. The illuminated area is 176 mm $\times$ 5 mm.

The confinement time of the light inside the cavity (and thus the enhancement factor) is given by the reflectivity R of the mirrors, by the losses through the coupling hole and other losses related with cavity "ears" and the optical surface rugosity. At 812 nm a reflectivity of 99.999% (10 ppm losses) can be reached. However due to the noisy and dusty environment of our setup and surface related problems we expect only a reflectivity $R^{\text{eff}} = 99.98\%$. The losses through the hole are calculated to be 1×10^{-4} leading to $R^{\text{eff}} = 99.97\%$. We can conservatively assume that the final effective reflectivity[3] (accounting also for losses at the "cavity-ear") will be $R^{\text{eff}} = 99.95\%$.

This effective reflectivity corresponds to $n_{\text{ref}} = 2000$ reflections between the two mirrors, leading to a lifetime of 170 ns. This large number of reflections results in a laser fluence enhancement, which can

[3]Note that we had $R^{\text{eff}} = 99.95\%$ at 6 μm with the "radioactive cavity" in 2003. High reflectivities are considerably more difficult to achieve at 6 μm than for 800-1000 nm.

be parametrized as:

$$F = f_t f_c \frac{n_{ref}}{A} \cdot E_{laser} \quad (24)$$

$$= 140 \text{ cm}^{-2} \cdot E \quad (25)$$

where E_{laser} is the Ti:Sa laser pulse energy, $A = 8.8$ cm^2 is the illuminated mirror surface, $f_t = 0.7$ is the transfer efficiency of the light from the laser output to the target cavity entrance (including all beam splitters required for laser monitoring etc.), and $f_c = 0.9$ is the coupling efficiency through the $\phi = 0.6$ mm diameter hole. For example, a pulse energy of 10 mJ at the Ti:Sa amplifier output will lead to an average laser fluence $F = 1.4$ J/cm^2.

One must compare this value with the *saturation* fluence given in Table 2. To avoid power broadening of the resonance lines we have to work at or below half of the saturation fluence. A laser pulse energy of 10 mJ is therefore sufficient.

7.5 Summary of setup modifications

Here we summarize all planned modifications of the apparatus and the expected costs. Even if we don't find suitably new LAAPDs we can still run with the existing LAAPDs, sacrificing 50% of the event rates in Tab. 2. The Ti:Sa laser modifications are straight-forward.

Table 3: *Setup modifications: 2009 vs. next beam time*

Item	Costs [kEUR]
Remove Raman cell	0
Ti:Sa optics (708 nm → 812 nm)	20
Beam transport optics (6 μm → 812 nm)	10
Multipass target cavity (6 μm → 812 nm)	30
Laser monitoring and calibration system in πE5	10
LAAPDs optimized for 8.2 keV, pre-amplifiers	35
^{3}He target gas	available
^{3}He gas handling system	10

In addition, we want to further improve the disk laser system, exploiting the rapid progress in disk laser technology. We expect a simpler disk laser system requiring less maintenance work during the beam time.

8 Expected event and background rates

The $\mu\,\mathrm{He}^+$ apparatus will be very similar to the one used for the muonic hydrogen Lamb shift experiment. Therefore we can base our estimation of signal and background event rates in the $\mu\,\mathrm{He}^+$ experiment on the rates measured in μp in the 2009 beam time.

In μp we measured 6 signal events per hour on resonance and 1 background event per hour, both for a proton beam current of 1900 μA.

8.1 Signal rate

The relevant parameters for the signal rate are summarized in Table 4. The $\mu\,\mathrm{He}^+$ experiment is considerably simpler than the one in μp due to the fact that the $\mu\,\mathrm{He}^+(2S)$ population is twice as large, at four times the target gas pressure, where the $\mu\,\mathrm{He}^+(2S)$ lifetime is still 70% larger. Higher target gas pressure results in 50% more muon stops inside the volume illuminated by the laser.

In the μp experiment we lost 98% of the laser pulse energy in the conversion between the red light from the Ti:sapphire laser to the required 6 μm wavelength (15 mJ in the red $\rightarrow$ 0.25 mJ at 6 μm). In the $\mu\,\mathrm{He}^+$ experiment we will directly use the Ti:sapphire light. This gain of ≈ 50 in pulse energy compensates for the increase in laser saturation fluence (see Tab. 2).

Table 4: *Comparison of signal rate between the measured* μp *transitions (at 1 mbar) and the proposed* $\mu\,^4\mathrm{He}^+$ *experiment (4 mbar). For* $\mu\,^3\mathrm{He}^+$ *the increase is smaller because of the smaller sub-level population (1/4 and 3/4 vs. 1) and weaker transition strength.*

Effect	μp	$\mu\,^4\mathrm{He}^+$	$\mu\,^4\mathrm{He}^+$ / μp
Long lived $2S$-population	1.1%	2.2%	2
$2S$ sub-level population	75%	100%	1.33
$2S$-lifetime (survival probability)	1 μs	1.7 μs	1.7
Muon stop in gas (trigger quality Q)	40%	60%	1.5
Muonic $2S$ atoms not drifting out of laser volume	80%	100%	1.25
Laser transition probability (only 20% for some weak transitions in $\mu\,^3\mathrm{He}^+$)	30%	30%	1
Laser repetition rate	500 s^{-1}	500 s^{-1}	1
Detection of Lyman alpha X-ray	70%	70%	1
Total event rate increase: for $\mu\,^4\mathrm{He}^+$			8
Total event rate increase: for $\mu\,^3\mathrm{He}^+$ strong transition and triplet population			6
Total event rate increase: for $\mu\,^3\mathrm{He}^+$ weak transition and singlet population			2

8.2 Background rate

The energy spectrum measured *without laser* in the 2009 μp beam time is shown in Fig. 6. It results from the sum of two main background sources for μp, only one of which is relevant for $\mu\,\mathrm{He}^+$, too:

- *Electrons from muon decay* give mostly signals above 10 keV, but some of this background is still present below 9 keV. The increase of this continuous background below 4 keV is due to

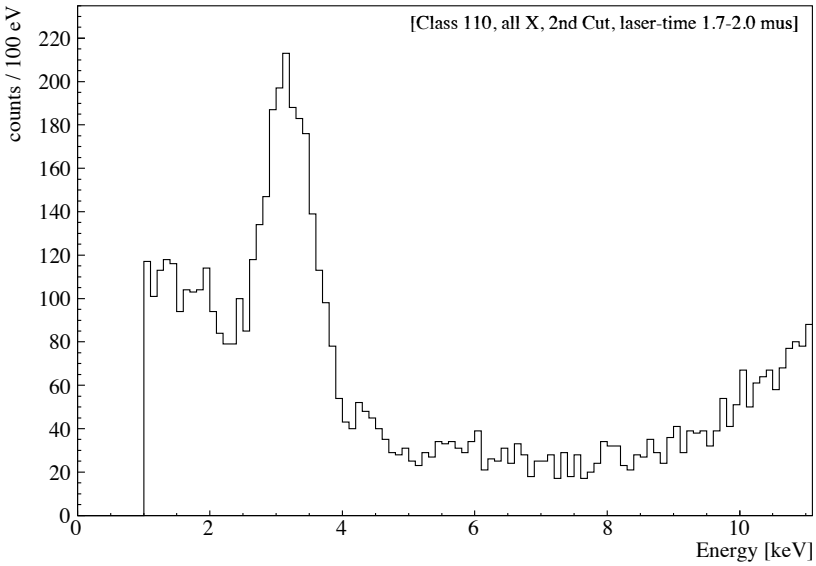

Figure 6: *X-Ray energy spectrum of events* in the laser time window *recorded in* $\boldsymbol{\mu}\mathbf{p}$ *during the 2009 beam time. The ratio between the background at 1.9 and 8.2 keV is approximately 3. The silver fluorescence peak at 3 keV stems from muon transfer from hydrogen to the silver-coated target walls. This background will not be present in* $\mu\,\mathrm{He}^+$ *(see text).*

Bremsstrahlung photons from decay electrons. As one can see, this μ-decay background is going to be smaller in the proposed $\mu\,\mathrm{He}^+$ experiment by a factor of 3.

- *Muon transfer to higher-Z atoms:* The peak at 3 keV in Fig. 6 is a peculiarity of our μp setup. We used silver-coated target windows, and muonic hydrogen atoms in the ground state, who drift to these windows, will transfer the muon to the silver coating. This transfer results in the silver fluorescence peak at 3 keV.
  Muon transfer from hydrogen to high-Z atoms is one of the main backgrounds in the μp experiment, but this will not occur in $\mu\,\mathrm{He}^+$, because the transfer reaction
  $\mu\,\mathrm{He}^+ + \mathrm{Z} \rightarrow \mu\mathrm{Z} + \mathrm{He}^+$ does not occur.

Other background sources in $\mu\,\mathrm{He}^+$ are:

- *"Second muons":* The prompt Lyman X-rays of a "second muon", which enters our apparatus (after the "first muon" opened the event gate and triggered the laser) fakes a delayed Lyman X-ray. The combined detection efficiency of our muon entrance detectors (ORed together) is as large as 94% (measured in 2009), and the second muon background is correspondingly reduced by 94%.
  This background will be the same for $\mu\,\mathrm{He}^+$ as for μp. It amounts to 0.1 ev/h.

- *Collisionally induced one-photon decay from the* $2S$ *state:* At 4 mbar He pressure the expected collisionally induced Stark deexcitation rate is $\sim 10^4\ \mathrm{s}^{-1}$. In the 200 ns long laser time window, we expect 0.1 ev/h.

- *Spontaneous two-photon decay from the* $2S$ *state:* The $2S$ state decays emitting two photons with a rate of $10^5\ \mathrm{s}^{-1}$, giving a broad continuous distribution. We expect that about 10% of these decays will fall into the Lyman-alpha energy cut and henceforth this background amounts to 0.1 ev/h.

As with the event rate estimations, the best way to estimate the background rate, is to reference it to the background rate measured in the μp case. In the run 2009 we have measured a background rate of 1 ev/h at 1.9 keV.

1. The decay-electron-induced background amplitude at 8.2 keV is only 1/3 of the background rate at 1.9 keV (see Fig. 6).
2. The Lyman-alpha width cut will increase by about a factor of 2, assuming that the LAAPD energy resolution will scale with the square root of the X-ray energy ($\sqrt{(8.2/1.9)} \approx 2.1$). So will the background rate.
3. Due to the better reflectivity of the cavity coating in the visible, the laser time window can be 1.5 times longer in $\mu\,\mathrm{He}^+$ compared to μp. The background increases by the same factor.
4. The muon stop rate will improve by a factor of 1.5 due to the higher target gas pressure. Both event rate and muon correlated background rate will increase by this factor.
5. The background related with the $2S$-state decay as presented above must be added.

This results in an expected background rate of:

$$1\,\mathrm{ev/h} \times 1/3 \times 2.1 \times 1.5 \times 1.5 \;+\; 0.1 + 0.1 = 1.8\,\mathrm{ev/h} \approx 2\,\mathrm{ev/h}.$$

8.3 Summary of expected rates

The conclusions about the event and background rate are summarized in Table 5. In the best case of $\mu\,^4\mathrm{He}^+$ we expect 48 events per hour and 2 background events per hour. The worst line in $\mu\,^3\mathrm{He}^+$ will have both signal and background rates a factor of two higher than the resonance lines measured in μp.
In μd we have observed additional background originating from *radiative* decay of $2S$ atoms at the level of about 1 event/hour, increasing the total background rate to ≈ 2 events per hour. This is the same level as expected for all lines in $\mu\,\mathrm{He}^+$.

Table 5: *Event and background rate summary. The number of events required to reach* $\Gamma/20$ *accuracy is 500.*

	$\mu\,^4\mathrm{He}^+$	$\mu\,^3\mathrm{He}^+$ (max)	$\mu\,^3\mathrm{He}^+$ (min)	μp (max)
Event rate on resonance:	48 ev/h	36 ev/h	12 ev/h	6 ev/h
Background rate:	2 ev/h for all $\mu\,\mathrm{He}^+$			1 ev/h

9 Systematics

The systematic effects which could shift the position of the resonance line has been extensively studied for muonic hydrogen. The following effects have been considered:

- AC-Stark shift
- DC-Stark shift
- Zeeman shift
- Pressure shift
- Doppler shift
- Laser energy asymmetry for blue/red detuning.

Apart from the laser energy blue/red detuning asymmetry, all the other effects are smaller than 50 MHz in μp. The same is valid for $\mu\,\mathrm{He}^+$. Generally speaking, all these effects are small because of the larger muon mass (*e.g.*, the Zeeman shift scales like $1/m$). Remember that we want to determine the centroid position with an accuracy of 20 GHz!

The only relevant systematic effect is given by a possible variation of the laser pulse energy at the various laser frequencies. A laser pulse energy asymmetry $A_{L/R}$ between measurements of the left and right wing of the resonance (red and blue detuned, respectively) will cause a shift of the line center by $\frac{1}{2}\,A_{L/R} \times \Gamma$. An asymmetry smaller than 3% must thus be achieved. This will result in a shift of the line position by $\sim 0.015\,\Gamma \;=\; 5\,\mathrm{GHz}$. Note that we aim for a statistical uncertainty of 20 GHz, and the systematic uncertainty should be ~ 3 smaller than the statistical one.

In conclusion, apart from the laser energy asymmetry for blue/red detuning there are no relevant systematics limiting our experiment. A detection system monitoring the light circulating in the cavity with a relative accuracy of 3% will be implemented in order to have control over the systematics effects on a level of $\Gamma/60$, *i.e.*, a factor of 3 better than the $\Gamma/20$ (50 ppm) accuracy we are aiming at.

10 Experimental program and milestones

The modifications of the apparatus, compared to the situation in 2009 for the μp Lamb shift experiment, are moderate. The main tasks to be done are listed in Table. 3. These modifications will be performed in 2010-2011.

As explained in the first section, it is preferable for this experiment to have long beam times (at least 14 weeks), starting immediately after a long (winter) shut-down of the PSI proton accelerator.

We propose to have a first beam time in April-July 2012 where we want to set up the apparatus and perform the measurements for Phase 1 in $\mu^4\mathrm{He}^+$, *i.e.* to search for the $2S_{1/2} - 2P_{3/2}$ resonance line and to measure both $2S - 2P$ transitions in $\mu^4\mathrm{He}^+$ to 50 ppm accuracy.

Assuming an uncertainty of the ^{4}He nuclear radius of up to 5 standard deviations of the value of Sick [11], there is an uncertainty of the first resonance line of 1.7 THz which corresponds to 5 natural line widths. The search for this line needs therefore measurements at 20 different wavelengths (2 hours each).

To avoid confusion about the measuring time required to scan the resonance we have to emphasize the following: to achieve the quoted number of 500 events in the resonance line, one has to measure for a time required to obtain 1000–1500 events, *if one measured all the time on the peak of the resonance*. This accounts for the fact that (a) the FWHM points are best to determine the centroid position and (b) that there is background. With the event rates given in Sec. 8 (48 events/hour on resonance for both transitions in $\mu^4\mathrm{He}^+$), an accuracy of 50 ppm ($= \Gamma/20$) will be reached after 30 hours of measuring time for each line. In practice we will need one week to scan the resonance (once it has been found). Time is spent for regular maintenance work (like filling LHe to the cryogenic magnets), but also for frequent laser frequency and energy calibrations. In addition, each change of laser wavelength required something like 15 minutes during the μp measurements. In $\mu\,\mathrm{He}^+$ one should change the laser wavelength frequently to minimize systematic effects.

In April-July 2013, we want to complete Phase 1 (if this was not already done in 2012) and perform Phase 2, the measurement of 5 transitions in $\mu^3\mathrm{He}^+$. The position of the first transition, $2S^{F=1}_{1/2} - 2P^{F=2}_{3/2}$, will probably not be known precisely and needs a search similar to the one for $\mu^4\mathrm{He}^+$. If one line is measured, the position of the other four lines can be predicted with sufficient precision.

The weaker line of $\mu^3\mathrm{He}^+$ has 12 events/hour. The corresponding measuring time will be 200 hours. The total measuring time for the five $\mu^3\mathrm{He}^+$ lines will thus be about 900 hours, corresponding to 8 weeks (considering off-times of the proton accelerator and parts of our apparatus).

The foreseen **milestones** are:

- **end 2010:** Analysis R98-03 measurements and publications, LAAPDs R&D, laser optimization.
- **end 2011:** Test of the whole laser system, multipass cavity and LAAPDs.
- **2012:** Setup of the apparatus in πE5 area, search and measure the two transitions in $\mu^4\mathrm{He}^+$ (Phase 1).
- **2013:** Complete measurements in $\mu^4\mathrm{He}^+$ if necessary, and measure the five transitions in $\mu^3\mathrm{He}^+$ (Phase 2).

11 Responsibilities of collaborating partners

12 Requests from PSI

13 Theory

In this section we present the theoretical background related with the $\mu\,\mathrm{He}^+$ experiment. It involves, from one side the bound-state QED theory in $\mu\,\mathrm{He}^+$ together with some nuclear structure related effects (like polarizability), and on the other side, the bound-state QED theory in H and He^+. A prediction (theory) of the Lamb shift in $\mu\,\mathrm{He}^+$ is clearly required in order to be able to perform the experiment (search for the resonance in the correct laser frequency region), and when the measurement is achieved, for the interpretation of the measured line position, *i.e.* extraction of the charge radii. Additionally a comparison between Lamb shift theory and measurements in $\mu\,\mathrm{He}^+$ will help to clarify the existence or not of a theoretical problem (discrepancy issue) in the muonic sector. The precise values of the He-isotopes charge radii are of fundamental importance in the interpretation of the He^+ spectroscopy. As we will present in full details below the knowledge of these radii open the way to check very challenging higher order bound-state QED terms.

In Sec. 3.5 we have presented the current $\mu\,\mathrm{He}^+$ theoretical prediction. Section 13.1 shows in a simplified way how to extract the $1S$ Lamb shifts and R_∞ from H and He^+ spectroscopy. Section 13.1.3 illustrates why the bound-state QED is interesting and presents the very interesting bound-state QED terms we aim to check. Finally in Section 13.2 a comparison between H and He^+ Lamb shifts is given. The emphasis here is set on the improved sensitivity of He^+ and $\mu\,\mathrm{He}^+$ spectroscopy compared to H and μp spectroscopy for the testing of interesting higher order bound-state QED corrections.

13.1 Bound-state QED test in H and He^+

Ultra-precise spectroscopy in simple systems like atomic hydrogen has been improved in recent years by several orders of magnitude in precision, according to the formidable progress of laser techniques. The $1S-2S$ transition frequency in H was measured at MPQ-Garching to a precision of 10^{-14} [35] using a cold hydrogen beam and the frequency comb laser invented at MPQ. Further improvements and extensions are in sight. This level of precision is appealing to test fundamental physics laws, in particular bound–state QED.

From the $1S-2S$ measurement and other measured transition frequency ($2S-8S\ldots$) [7] in H the $1S$ Lamb shift was extracted. Prior to our measurement in μp, the comparison of this experimentally determined Lamb shift with the theoretical prediction was limited by the poor knowledge of the proton rms radius r_p. From the measurement of the $2S-2P$ energy difference in μp to 20 ppm a proton radius of $r_\mathrm{p}=0.841(1)$ fm ($u_r=10^{-3}$) was deduced [34]. This will improve the achievable level of the bound-state QED test from 6×10^{-6} to 3×10^{-7} as soon as the above mentioned discrepancy problem is solved. Then, then uncertainty of the Rydberg constant ($R_\infty=\alpha^2 m_e c/2h$) will also be reduced by an order of magnitude.

A measurement of the $1S-2S$ transition frequency in He^+ ions is even more promising because the interesting QED terms scale with $Z^{5\ldots7}$ and thus become larger for He^+ than H, relative to the measured $2S-1S$ energy difference which scales with Z^2. By measuring the $1S-2S$ transition frequency in He^+ and knowing the R_∞ from H spectroscopy it is possible to deduce the $1S$ Lamb shift in He^+. As in the H case, a precise value of the nuclear rms charge radius is required in order to compare the theoretical prediction of the $1S$ Lamb shift in He^+ with the measured one.

13.1.1 Experimental $1S$ Lamb shift in H and comparison with theory

The energy levels of hydrogen-like atoms are described in a simplified way by

$$E=\frac{Z^2}{n^2}R_\infty\frac{m_r}{m}+L(\alpha,c,r_x\ldots)$$

where R_∞ is the Rydberg constant, m_r the reduced mass of the system, m the electron mass, α the fine structure constant, r_x the nuclear rms charge radius, Z the nuclear charge and L the Lamb shift. The Lamb shift is defined as any deviation of the energy level from the prediction of the Dirac (Schrödinger) equation caused by radiative (QED), recoil and nuclear structure corrections (see Sec. 13.2 for a more precise definition). Note that to predict the hydrogen energy levels within bound–state QED, we need to know, with proper accuracy, fundamental constants like R_∞, α, $\hbar$, $m\ldots$ and r_p.

Several transition frequencies measured in hydrogen and deuterium have been combined to determine the hydrogen $1S$–Lamb shift and R_∞ [2]:

$$\left.\begin{array}{rcl} \Delta E_{1S-2S} &=& 0.75\,R_\infty \frac{m_r}{m} - L_{1S} + L_{2S} \\ \Delta E_{2S-8S/D} &=& 0.23\,R_\infty \frac{m_r}{m} - L_{2S} + L_{8S/D} \\ & \ldots & \\ L_{nS} &=& \frac{1}{n^3} L_{1S} + \varepsilon_n \end{array}\right\} \Rightarrow \left\{\begin{array}{rcl} L_{1S}^{\mathrm{exp}} &=& 8172.839\,(22)\ \mathrm{MHz} \\ cR_\infty &=& 3\,289\,841\,960.362\,(25)\ \mathrm{MHz} \end{array}\right.$$

Progress in H-atom spectroscopy will further reduce the quoted experimental errors of L_{1S}^{exp} and R_∞ in the near future.

Bound–state QED can predict the value of the Lamb shift (L_{1S}^{th}). Its uncertainty is related by the inadequacy of the theory itself (first uncertainty in the following equations) and by the uncertainty related to the fundamental constants (second uncertainty, given by the uncertainty of r_p) [2, 47, 40, 46, 39, 56, 41, 42, 43, 44, 45, 48, 12]:

$$\left.\begin{array}{r} r_\mathrm{p} \\ \alpha,\ c,\ \hbar,\ m\ldots \\ \mathrm{QED} \end{array}\right\} \Rightarrow L_{1S}^{\mathrm{th}} = 8172.900\,(4)^{\mathrm{th.}}(51)^{\mathrm{fin.\ size.}}\ \mathrm{MHz}, \quad r_\mathrm{p} = 0.895\,(18)\ \mathrm{fm\ from\ e–p\ scattering}$$

$$L_{1S}^{\mathrm{th}} = 8172.743\,(4)^{\mathrm{th.}}(3)^{\mathrm{fin.\ size.}}\ \mathrm{MHz}, \qquad r_\mathrm{p} = 0.841\,(1)\ \mathrm{fm\ from}\ \mu\mathrm{p\ Lamb\ shift}$$

As can be inferred from the above equations, prior to the successful μp Lamb shift experiment the comparison between theory and experiment was strongly limited by the uncertainty of the proton radius to a level of 6×10^{-6}. The determination of r_p by the muonic hydrogen Lamb shift experiment has opened the way to check bound-state QED on a level of 3×10^{-7}. However, first it is necessary to solve the discrepancy problem between the Lamb shift predicted using r_p from the μp experiment and the experimentally determined L_{1S}^{exp}.

13.1.2 Experimental $1S$ Lamb shift in He^+ and comparison with theory

A similar comparison between theoretically predicted and experimentally determined $1S$-Lamb shift in He^+ will be reached when both the proposed $\mu\,\mathrm{He}^+$ and the ongoing He^+ spectroscopy experiments will be accomplished. The situation will be even much better, first because we are more sensitive to the interesting bound-state QED contributions and second because we will have an independent very sensitive way to determine R_∞.

When the $1S-2S$ transition frequency in He^+ will be measured with $u_r = 2 \times 10^{-14}$ [9], the $1S$-Lamb shift in He^+ can be deduced by knowing R_∞ from the H-spectroscopy experiments as:

$$\left.\begin{array}{rcl} \Delta E_{1S-2S} &=& 0.75 \cdot 2^2 \cdot R_\infty \frac{m_r}{m} - L_{1S} + L_{2S} \\ L_{nS} &=& \frac{1}{n^3} L_{1S} + \varepsilon_n \\ R_\infty && \text{from H spectroscopy} \end{array}\right\} \Rightarrow\ L_{1S}^{\mathrm{exp}} \quad \text{expected uncert.=0.088 MHz}$$

This can then be compared with the theoretical prediction [41, 48, 55, 12]:

$$\left.\begin{matrix} r_{\rm He} \\ \alpha,\ c,\ \hbar,\ m\ldots \\ \text{QED} \end{matrix}\right\} \Rightarrow \begin{cases} L_{1S}^{\rm th} = 107693.196\,(211)^{\rm th.}(348)^{\rm fin.\ size.}\ \text{MHz}, & r_{\rm He} = 1.681\,(4)\ \text{fm} \quad \text{from scatt.} \\ L_{1S}^{\rm th} = 107693.yyy\,(211)^{\rm th.}(\ 40)^{\rm fin.\ size.}\ \text{MHz}, & r_{\rm He} = 1.6xxx\,(5)\ \text{fm} \quad \text{from } \mu\,\text{He}^+ \end{cases}$$

As in the hydrogen case, comparison between theoretical and experimental $1S$ Lamb shift in He^+ will be limited by the uncertainty related with the nuclear rms charge radius. This is the main motivation for the $\mu\,\text{He}^+$ experiment.

13.1.3 Why is bound-state QED interesting?

Precision QED for free particles (*e.g.*, $g-2$) is being calculated with an increasing number (several thousands) of complicated diagrams (up to the five–loop level [38]). Bound–state QED deals with diagrams up to the two–loop level in α (few contributions to the three-loop), but the charged particles are bound, leading to the presence of Coulomb exchange ($Z\alpha$ expansion) that is difficult to calculate. Free QED involves only one small parameter α, while bound–state QED needs at least three expansion parameters α, $Z\alpha$ and m/M:

- α, the power of which indicates the number of QED loops.
- $Z\alpha$ is the Coulomb strength. It represents the binding effect. α and $Z\alpha$ expansions behave quite differently. There is a number of contributions where we need to sum over an infinite number of Coulomb exchanges, like for the Bethe logarithm. If $Z\alpha$ is not small (Uranium: $Z\alpha \approx 0.7$), there is strong coupling, and perturbation theory can not be applied. For $Z\alpha \to 0$ there is a non–analytic behavior of the perturbation theory. The result is the occurrence of numerous logarithms $\ln^i[(Z\alpha)^{-2}]$ and large coefficients in the expansion.
- m/M is the recoil parameter. In the non–relativistic case the two-body system can be exactly solved by introducing the reduced mass of the system, but the separation of center–of–mass and relative motion can not be done in a relativistically covariant way. This complicates the treatment of bound–states fundamentally.

The QED corrections to the energy levels can be written in the form of a power series expansion in these three small dimensionless parameters. These parameters, in particular α and $Z\alpha$, enter both in the wave function and the particle propagator in a non-perturbative way. Although bound–state QED is non-perturbative, it is possible to make use of these small parameters to develop expressions in increasing order of smallness. However the non-perturbative nature of this expansion shows up in the coefficients of the power series. Some of these coefficients are not constants but slowly varying functions (*e.g.* $\ln\,(Z\alpha)^{-2}$ in Eq. (27)) of the expansion parameters. Hence the energy shift caused by a given kernel can not be estimated by simply counting the powers in α and $Z\alpha$ it contains.

To get an idea of the difference between a bound and a free electron propagator consider the self–energy diagram for a free and a bound electron:

$$S_F(q) = \frac{i}{\not{q} - m}$$ 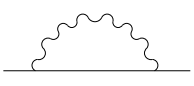

$$S_B(q) = \frac{i}{\not{q} - m - \gamma^0 V}$$ 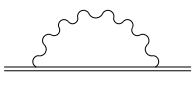

For high energies of the exchanged virtual photon, the Dirac–Coulomb (bound electron) propagator may be expanded as

$$\frac{1}{\not q - m - \gamma^0 V} = \frac{1}{\not q - m} + \frac{1}{\not q - m}\gamma^0 V \frac{1}{\not q - m} + \frac{1}{\not q - m}\gamma^0 V \frac{1}{\not q - m}\gamma^0 V \frac{1}{\not q - m} + \cdots$$

where $V = \frac{Z\alpha}{r}$, r $\sim (Z\alpha)$.
In terms of Feynman diagrams this corresponds to the following expansion:

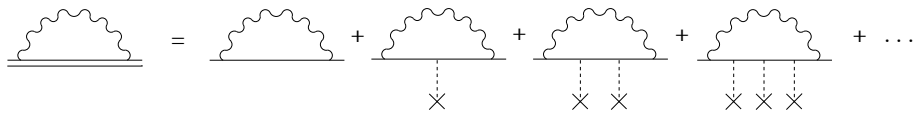

In the bound–state QED problem, every coefficient of the α expansion is developed in powers of $Z\alpha$ as shown for the one-loop self–energy in the above figure. Every additional photonic line connecting the electron to the nucleus generates an additional power in $Z\alpha$.

13.1.4 An example: One-loop self–energy in hydrogen and hydrogen-like atoms

The one-loop corrections (order of α) are by several orders of magnitude the largest contributions to the Lamb shift and are given by the electron self–energy and the vacuum polarization. In the following, focus is given on the evaluation of the self–energy term which is the most problematic and largest contribution to the Lamb shift in hydrogen. Because of the approximate $(Z\alpha)^4/n^3$ scaling law of the self–energy level shift, it is convenient to express the energy shift of each state caused by the one-loop self–energy as

$$\Delta E_{SE}^{(\mathrm{one-loop})} = m\frac{\alpha}{\pi}\frac{(Z\alpha)^4}{n^3}F_n(Z\alpha). \tag{26}$$

There exist two ways to calculate $F_n(Z\alpha)$. The first relies on a perturbative expansion of the Dirac–Coulomb propagator on $Z\alpha$, *i.e.,* the coupling constant to the external field [51, 39, 40, 41, 42], and the second one treats the Dirac–Coulomb propagator exactly [43, 44, 45, 46, 47, 48]. The coupling constant $Z\alpha$ for heavy elements (*e.g.*,, for uranium $Z\alpha \simeq 0.7$) is not really small compared to 1. For high-Z nuclei the semi–analytical expansion of $F_n(Z\alpha)$ in terms of $Z\alpha$ and $\ln(Z\alpha)$ no longer converges, and in that case $F_n(Z\alpha)$ must be evaluated with the numerical all–order exact method. Hence the perturbative method is valid only for low–Z ($Z \leq 5$ for the one-loop self–energy) systems (but the exact value is needed for accuracy in the region of a few Hertz, even for Z=1).

In the perturbative approach the dimensionless quantity $F_n(Z\alpha)$ can be expressed as a semi–analytical expansion over $Z\alpha$ and $\ln(Z\alpha)$,

$$\begin{aligned} F_n &= A_{40} + A_{41}\ln(Z\alpha)^{-2} + (Z\alpha)A_{50} \\ &\quad + (Z\alpha)^2\left[A_{62}\ln^2(Z\alpha)^{-2} + A_{61}\ln(Z\alpha)^{-2} + G_{SE}(Z\alpha)\right] \end{aligned} \tag{27}$$

The first index of the A coefficients gives the power of $Z\alpha$ (including the $(Z\alpha)^4$ pre–factor in Eq. (26)), whereas the second index corresponds to the power of the logarithm. $F_n = F_n(nlj, Z\alpha)$ and $A_{pq} = A_{pq}(nlj)$ depend on the atomic state with quantum numbers n, l, j. The work involved in calculating the A constants in Eq. (27) has involved many physicists and has extended over more than five decades. A complete list of the A coefficients is given in [2]. A_{40} contains the Bethe–logarithm $\ln(k_0(nl))$, and the self–energy remainder function $G_{SE}(Z\alpha)$ contains the higher order contribution in $Z\alpha$ to the one-loop self–energy and can be semi–analytically expanded as [49]

$$\begin{aligned} G_{SE}(Z\alpha) &= A_{60} + (Z\alpha)\left[A_{71}\ln(Z\alpha)^{-2} + A_{70}\right] \\ &\quad + (Z\alpha)^2\left[A_{83}\ln^3(Z\alpha)^{-2} + A_{82}\ln^2(Z\alpha)^{-2} + A_{81}\ln(Z\alpha)^{-2} + A_{80}\right]. \end{aligned} \tag{28}$$

The higher–order terms in the potential expansion of the Dirac–Coulomb propagator and the relativistic corrections to the wave–function both generate higher order terms in $Z\alpha$ which are manifest in Eqs. (27) and (28).

Since the binding Coulomb field enters in a non-perturbative way and no closed–form expression for the Dirac–Coulomb propagator exists, already the calculation of corrections of $(Z\alpha)^2$ relative order is a highly non trivial task. The one-loop electron self–energy contributes to all orders in $Z\alpha$, and the separation in $(Z\alpha)^2$ relative contribution involves hundreds of terms. Additionally the series expansion in $Z\alpha$ is slowly convergent.

The best evaluation of the G_{SE} term is hence based on a direct all–order numerical evaluation of the bound–electron propagator [50]. Calculating F_n in the all–order exact method and subtracting from it all the other contribution related to the A coefficients of Eq. (27) gives G_{SE}. The uncertainty of the one-loop self–energy to a given energy level arises entirely from the uncertainty of the G_{SE}. The non-perturbative results are consistent with the results of the $Z\alpha$–expansion but are orders of magnitude more precise. The numerical uncertainty of the all–order calculation is $0.8 \times Z^4$ Hz [46], whereas the uncertainty related to the perturbative method is of 28 kHz, due to the truncation of the $Z\alpha$ expansion (unevaluated higher order terms). The numerical all–order (non perturbative) treatment of the one-loop self–energy for hydrogen has nowadays overcome the limitations of the perturbative approach in $Z\alpha$ [46].

13.1.5 The present limit of theory: Two-loop self–energy in hydrogen

Among all the "pure" QED contributions to the Lamb shift only the two-loop terms have a non-negligible uncertainty [56, 57]. The two-loop self–energy shift can be expressed as:

$$\Delta E_{SE}^{(\text{two-loop})} = m\Big(\frac{\alpha}{\pi}\Big)^2 \frac{(Z\alpha)^4}{n^3} G_n(Z\alpha). \tag{29}$$

As for the one-loop self-energy, in recent years, intensive studies of the higher-order two-loop corrections to the Lamb shift have been performed, with two different methods: the all-order approach [12] and the expansion in powers of $Z\alpha$ and $\ln[(Z\alpha)^{-2}]$. In the perturbative approach the function $G_n(Z\alpha)$ can be expanded as

$$\begin{aligned} G_n &= B_{40} + (Z\alpha)B_{50} \\ &\quad + (Z\alpha)^2 \left[B_{63} \ln^3 (Z\alpha)^{-2} + B_{62} \ln^2 (Z\alpha)^{-2} + B_{61} \ln (Z\alpha)^{-2} + G_{h.o}\right] , \end{aligned} \tag{30}$$

with $G_{h.o.} = B_{60} + (Z\alpha)(\ldots)$. The calculation of the B coefficients [51, 39, 41, 52, 53, 54, 55] is at present one of the most challenging problems in bound–state QED, and it is the limiting factor of the theory. B_{40} which is the leading–order correction is quite small, $B_{40}(ns) = 1.409244$, whereas B_{50} was also found to be large, $B_{50}(ns) = -24.2668(31)$. This indicates a slow convergences or even a non-perturbative behavior of the two-loop contributions. The B_{6i} coefficients have turned out to be surprisingly large, with a remaining contribution to B_{60} due to high-energy virtual photons still being investigated ($B_{63}(ns) = -8/27$, $B_{62}(ns) = -16/27 - (16/9)\ln 2$, $B_{61}(ns) = 48.388913$, $B_{60}(ns) = -61.6(9.2)$ [12]). The convergence of this expansion is rather modest, and non-negligible contributions from unknown B_{7i}-terms cannot be excluded. Higher order corrections in $Z\alpha$ are required, but the complexity of calculations of order $\alpha^2(Z\alpha)^7$ does not seem to make it feasible in the near future. Hence the estimation of uncertainty of higher order effects is rather problematic.

A non-perturbative approach in the parameter $Z\alpha$ is therefore desirable even for hydrogen and helium ($Z = 1, 2$), but up to now this numerical approach is reliable only for ions with $Z \geq 10$. Non-perturbative all-order calculations were performed first at high Z and recently down to $Z = 10$, and then extrapolated to $Z = 1$. The result differs from the perturbative approach by nearly 6 kHz

for the two-loop Lamb shift in H, and following common practice (see also the discussion in Ref. [55]), we take half of this discrepancy as uncertainty, resulting in 3 kHz uncertainty. Obviously, these terms become quite large for He^+ because they scale as Z^6 and higher powers. Figure 7 shows the $G_{h.o.}$ term for hydrogen calculated for $Z = 1$ with the perturbative expansion (which is B_{60}), compared with the $G_{h.o.}$ values from the all–order approach at $Z \geq 10$. Simple extrapolation of the all–order values to $Z = 1$ is in obvious discrepancy with the value calculated by perturbative expansion. Effort to solve this discrepancy is required.

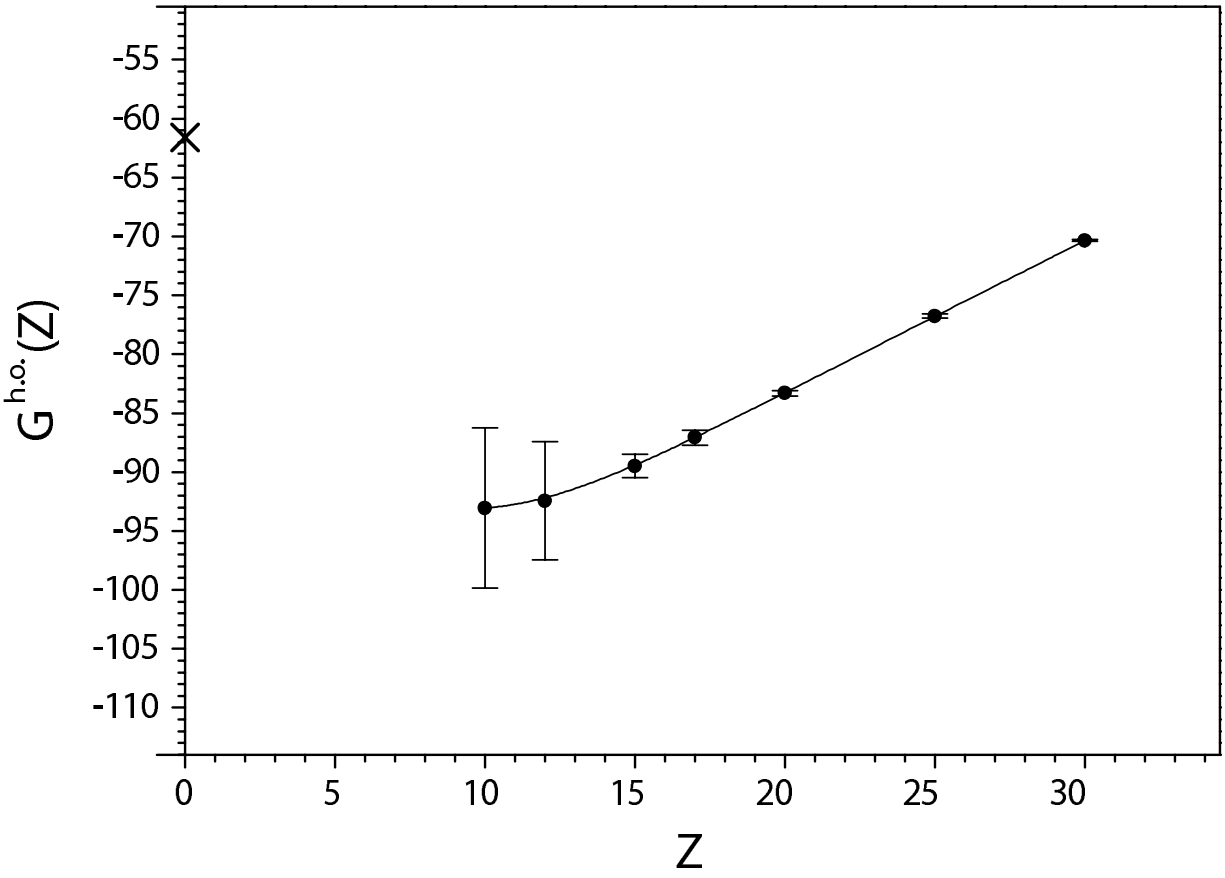

Figure 7: *$G_{h.o.}$ term calculated with the perturbative approach in $Z\alpha$ shown with a cross point, and the all–order approach for higher Z (other points). In order to obtain the $G_{h.o.}$ values from the all–order approach, the various known B's from Eq. 30 calculated with perturbation theory have to be subtracted from G_n. The extrapolation from higher Z (non-perturbative) to $Z = 1$ gives $G_{h.o.} = 101(15)$, in discrepancy with the value $B_{60} = -61.6$ from perturbative calculations.(Figure from [12])*

The expansion of the two-loop self–energy in powers of $Z\alpha$ and $\ln[(Z\alpha)^{-2}]$ leads to surprisingly large terms and is therefore considered as prototype for badly converging series. Bad convergence of the $(Z\alpha)$ expansion and disagreement between the perturbative and non-perturbative approach require progress in this field, both from the theoretical and experimental side. Bound–state QED may be considered a platform for the development of instruments to understand bound–state systems where no expansion in small parameters is possible. For the verification of this challenging two-loop contributions in H and He^+ a better knowledge of the proton radius (already achieved) and of the alpha-particle radius are required.

13.2 H and He^+ Lamb shift theory and verification

In Table 6 we summarize all contributions and some important quantities which are relevant for the $1S-2S$ transition in H and He^+. The total energy difference $\Delta E_{2S-1S} = E_{2S} - E_{1S}$ given on row (A) is the $1S-2S$ transition energy. This energy difference is essentially given by $3/4\,Z^2\,R_\infty\,m/m_r$. Corrections related to QED, relativistic and nuclear structure effects affect this energy difference at the few ppm level. The uncertainty of the ΔE_{2S-1S} prediction caused by the uncertainty of R_∞ is given in row (B) and is $\approx 3/4\,\delta R_\infty$. Present knowledge of R_∞ ($\delta R_\infty/R_\infty = 6.6\times10^{-12}$) comes mainly from precision spectroscopy of H($1S-2S$), H($2S-8D$), H($2S-12D$)[7].

We define the Lamb shifts L_{1S} and L_{2S} according to the generally adopted convention that a part of the recoil corrections, which are beyond the Dirac energy value but do not lift the $2S_{1/2}-2P_{1/2}$ degeneracy, as well as hyperfine effects, are excluded from the definition of the Lamb shift L. The following, implicit definition [61] is the commonly adopted one, and reads

$$E = c^2 m_{\rm r}\,[f(n,j)-1] - \frac{c^2 m_{\rm r}^2}{2(m_{\rm e}+M)}\,[f(n,j)-1]^2 + L + E_{\rm hfs}\,. \tag{31}$$

Here, E is the energy level of the bound two-body system (electron+nucleus), and $f(n,j)$ is the dimensionless Dirac energy. E.g., we have $f(1,\frac{1}{2}) = f(1S) = \sqrt{1-(Z\alpha)^2}$, and $f(2,\frac{1}{2}) = f(2S) = \sqrt{\frac{1}{2}\,(1+\sqrt{1-(Z\alpha)^2})}$ for the $1S$ and $2S$ states, respectively. The other symbols are as follows: $m_{\rm r}$ (M) is the reduced mass of the system, M the nuclear mass, and $E_{\rm hfs}$ is the energy shift due to hyperfine effects. The latter is absent for a nucleus with spin 0 (^{4}He).

The Lamb shift difference $L_{1S}-L_{2S}$ can be determined to essentially the same absolute precision in frequency units as the Rydberg constant using this simplified expression:

$$(L_{1S}-L_{2S})^{\rm exp} \approx \Delta E_{2S-1S} - 3/4 Z^2 R_\infty. \tag{32}$$

In fact ΔE_{2S-1S} in H is measured to an accuracy of 1.4×10^{-14} [35], much better than R_∞, and similarly when the measurement in He^+ will be finished. The experimentally inferred Lamb shift difference $(L_{1S}-L_{2S})^{\rm exp}$ is given in row (C) whereas the theoretical predicted one, $(L_{1S}-L_{2S})^{\rm th}$ in row (E). The relative uncertainty of the theoretical predictions is shown in row (F). For these theoretical predictions we made use of nuclear radii values coming from independent experiments like electron scattering experiments, *e.g.*, $r_p = 0.895 \pm 0.018$ fm, $r_{^4{\rm He}} = 1.681(4)$ fm [11].

The quoted theoretical uncertainties for the Lamb shift differences $L_{1S}-L_{2S}$ in H and He^+ take into account the recent investigations reported in Refs. [41, 55, 58] for H and in Ref. [57] for He^+. The theoretical uncertainties of these calculated Lamb shift differences result from quadratically adding the uncertainties of the nuclear-size term and computational uncertainties. Note that we did not use the newly determined $r_{\rm p}$ from μp.

The resulting relative uncertainty in He^+ of 3.7 ppm ($\pm$348 kHz) is roughly half the size as the corresponding value in hydrogen (6.3 ppm or $\pm$44 kHz) and is composed in almost equal parts from uncertainties of the nuclear size and computational uncertainties. This is in sharp contrast to the situation in hydrogen.

The main contribution to the Lamb shifts in H and He^+ are given by the one-photon one-loop self-energy which scales approximately like $\alpha(Z\alpha)^4$. Detailed calculation shows that this term scales according to $\alpha(Z\alpha)^4\ln[(Z\alpha)^{-2}]$. Both at $Z=1$ and at $Z=2$, the dependence on Z can be approximated by a non-integer power $\approx Z^{3.7}$.

Among all the "pure" QED contributions to the Lamb shifts only the two-loop terms have a non-negligible uncertainty. The contribution of the most critical terms (B_{60} and B_{7i}) together with its uncertainty is given in row (G) of the Table. It is interesting to observe that the uncertainty of the

Table 6: *Comparison of the energy differences (in frequency units) between the $1S$ and $2S$ states of the H atom and He^+ ion, given for the binding energy E, the Lamb shift L, some higher order QED terms, and for the energy shifts due to the nuclear size and polarizability. Uncertainties are given in parenthesis.*

		H($1S-2S$) [kHz]	He^+($1S-2S$) [kHz]	ratio
A	ΔE_{2S-1S}	2.466×10^{12}	9.869×10^{12}	Z^2
B	$\delta\Delta E^{\rm th}_{2S-1S}$ (from δR_∞)	$(16)^a$	$(65)^a$	Z^2
C	$(L_{1S}-L_{2S})^{\rm exp}$	7 127 831(16)		Z^2 (Eq. (32))
D	$\delta(L_{1S}-L_{2S})^{\rm exp}$ (from δR_∞)	*2.2 ppm*^{a}	*0.7 ppm*^{a}	
E	$(L_{1S}-L_{2S})^{\rm th}$	7 127 887(44)	93 856 127(348)	$Z^{3.7}$
F	$\delta(L_{1S}-L_{2S})^{\rm th}$	*(6.3 ppm)*	*(3.7 ppm)*	
G	B_{60} and B_{7i} terms	$-8(3)$	$-543(185)$	$Z^{6...}$
H	other uncalc. higher terms (C_{50}, recoil...)	$\sim(2)$	$\sim(100)$	$Z^{5...7}$
I	nuclear size (p, ^{4}He)	$1102(44)^b$	$62\,079(295)^c$	$Z^4 r^2$
J	uncert. of nucl. size (from μp, μ^4He$^+$)	(2)	$(40)^d$	
K	nucl. polarizability	$-0.06(2)^e$	$-28(3)^f$	
L	$1S-2S$ laser linewidth	<1	$\sim 13^g$	
M	$1S-2S$ natural linewidth	0.0013	0.084	Z^6

(a): will be reduced by a factor 2 when measuring, e.g., H($1S-3S$) to 1 kHz precision
(b): with r(p) = 0.897(18) fm [3]
(c): with $r(^4\mathrm{He}) = 1.681(4)$ fm [11]
(d): if the nuclear polarizability of μ^4He($2S$) can be calculated to 5% uncertainty
(e): calculated, see Eq. (A11) of Ref. [1]
(f): calculated, see Ref. [59]
(g): expected

$1S-2S$ prediction due to δR_∞ in comparison to the higher-order two-loop effects is 16 times larger for H than for He^+ because the two-loop effects scale like Z^6.

The largest uncertainty in the prediction of the Lamb shifts in H and He^+ is given by the finite size effect. Line (I) reports the finite size contributions and uncertainties for nuclear radii extracted from electron scattering experiments. However the uncertainties of the nuclear radii can be reduced by an order of magnitude via the Lamb shift measurements in μp and $\mu\,\mathrm{He}^+$. Row (J) shows the uncertainties of this finite size contribution after the performed measurement in μp, and for He^+ the expected results after completion of the corresponding measurements in $\mu\,\mathrm{He}^+$. Other source of uncertainties are given by the nuclear polarizability effects whose contribution is shown in row (K). We note that the nuclear polarizability correction for $^4He^+$ has been computed very recently for the first time [59]. The correction is numerically significant on the precision level which may be reached in the not-too distant future.

By looking at the Table we can draw following conclusions:

- *Hydrogen*: Prior to the measurement of the Lamb shift in μp the bound-state QED test was limited to a level of 6×10^{-6} level by the uncertainty related with the rms proton radius. After the μp measurement we have opened the way to check bound-state QED ($1S$ Lamb shift prediction) to a level of 3×10^{-7}. To reach such an accuracy an improvement of R_∞ is required (some improvement of the R_∞ uncertainty can be achieved by the ongoing $1S-3S$ measurement in H). It has to be stressed here that before being able to perform such a precision test we need to understand the above explained discrepancy.

- *Helium*: Due to scaling of the interesting QED corrections with high powers of Z, He^+ offers promising opportunities in comparison to H. The comparison between theoretical and experimental $1S$-Lamb shift in He^+ is more sensitive to interesting two-loop correction (scaling with Z^6) and less to the uncertainty of the Rydberg constant (which scales like Z^2). The number of theoretical digits that can be compared with experiments is about the same in hydrogen and He^+. The scaling of the limiting contributions with Z^6 compared with the scaling of the Bohr structure (Rydberg) Z^2 means that the same interesting terms are tested with on order of magnitude more precision in He^+ than in H.

  For example the B_{60} term can be checked with an accuracy of 50 kHz. This has to be compared with the difference between the predictions from the two developed approaches (all-order, expansion) of $\sim$ 400 kHz.

13.3 Impact on nuclear theory of few nucleon nuclei

We have seen in the previous chapter the relevance of the $\mu\,He^+$ experiment for the interpretation of the spectroscopy in hydrogen-like atoms. It will lead to a possible understanding of the discrepancy, an accurate test of QED, and improvement of R_∞. Additionally the nuclear radii extracted from the $\mu\,He^+$ Lamb shift may be used in nuclear physics. Precise isotope shift measurements of ^{3}He, ^{6}He, ^{8}He [13] have been accomplished by means of laser spectroscopy which provide accurate differences of the rms radii relative to ^{4}He. To deduce absolute radii it is therefore necessary to deduce the absolute radius of the reference isotope ^{4}He. Our μp, μd and $\mu\,^{3,4}He^+$ experiments will lead to a determination of the proton, deuteron, ^{3}He ^{4}He, ^{6}He, ^{8}He rms charge radii.

The knowledge of these radii will provide additional useful observables to check theories (NN, NNN, NNNN potentials) of few nucleons nuclei[14].

A measurement of two transitions in ^{3}He (one starting from the singlet and one from the triplet $2S$ state) will lead to a determination of the hyperfine splitting, and thus to the Bohr-Weisskopf contribution. A measurement of the two transitions with 50 ppm will lead to the knowledge of the quadratic sum of rms charge and magnetic radius in ^{3}He with 1% accuracy. This is another observable which may be used to check nuclear models.

References

[1] CODATA-02: P. J. Mohr and B. N. Taylor, Rev. Mod. Phys. **77**, 1 (2005).

[2] CODATA-06: P. J. Mohr, B. N. Taylor and D. B. Newell, Rev. Mod. Phys. **80**, 633 (2008).

[3] P. G. Blunden and I. Sick, Phys. Rev. C **72**, 057601 (2005).

[4] P. Wang et al., Phys. Rev. D **79**, 094001 (2009).

[5] I. Sick, Phys. Lett. B **576**, 62 (2003).

[6] J. Flowers et al., IEEE Trans. Instr. Meas. **56**, 331 (2007).

[7] B. de Beauvoir et al., Eur. Phys. J. D, **12**, 61 (2000).

[8] J. C. Bernauer et al., Can. J. Phys. **85**, 419 (2007).

[9] M. Herrmann et al., Phys. Rev. A **79**, 052505 (2009).

[10] C. Gohle et al., Nature **436**, 234-237 (2005)

[11] I. Sick, Phys. Rev. C **77**, 041302 (2008).

[12] V. A. Yerokhin, Phys. Rev. Lett. **80**, 040501(R) (2009).

[13] P. Mueller et al., Phys. Rev. Lett. **99**, 252501 (2007)

[14] E. Caurier et P. Navrátil, Phys. Rev. C **73**, 021302(R) (2006)

[15] H.P. von Arb *et al.*, Phys. Lett. B **136**, 232 (1984).

[16] F. Dittus, Ph. D. thesis 7877, ETH Zurich (1985).

[17] R. Bacher, Z. Phys. A **315**, 135 (1984).

[18] G. Carboni *et al.*, Nucl. Phys. A **278**, 381 (1977).

[19] G. Carboni *et al.*, Phys. Lett. B **73**, 229 (1978).

[20] M. Eckhause *et al.*, Phys. Rev. A **33**, 1743 (1986).

[21] H. Orth, in *Electromagnetic Cascade and Chemistry of Exotic Atoms*, ed. by L. Simons *et al.* (Plenum, New York, 1990), p. 155.

[22] P. Hauser *et al.*, Phys. Rev. A **46**, 2363 (1992).

[23] L.M.P. Fernandes et al., Journal of Instrumentation **2**, 08005 (2007).

[24] L. Ludhova et al., Nucl. Instrum. and Meth. A **540**, 169 (2005).

[25] A. Antognini, Ph.D. thesis, LMU Munich (2005).

[26] L. Ludhova, Ph.D. thesis, University of Fribourg (2005).

[27] A. Antognini et al., Opt. Com. **253**, 362 (2005).

[28] A. Antognini et al., IEEE J. Quant. Electr. **45**, No. 8, 993 (2009).

[29] A. P. Martynenko, Phys. Rev. A **76**, 012505 (2007).

[30] K. Pachucki, Private communication.

[31] E. Borie and G.A. Rinker, Phys. Rev. A **18**, 324 (1978).

[32] E. Borie Z. Physik A **297**, 17 (1980).

[33] G.A. Rinker, Phys. Rev. A **14**, 18 (1976).

[34] R. Pohl et al., to be submitted to Nature (2010).

[35] M. Niering et al., Phys. Rev. Lett. **84**, 5496 (2000).

[36] T. Suzuki, T. F. Measday, and J. P. Roalsvig, Phys. Rev. C **35**, 2212 (1987).

[37] R. Pohl et al., Phys. Rev. Lett. **97**, 193402 (2006).

[38] T. Kinoshita and M. Nio, Phys. Rev. D **73**, 053007 (2006).

[39] K. Pachucki, Phys. Rev. A **63**, 042503 (2001).

[40] U. D. Jentschura and K. Pachucki, Phys. Rev. A **54**, 1853 (1996).

[41] K. Pachucki and U. D. Jentschura, Phys. Rev. Lett. **91**, 113005 (2003).

[42] U. D. Jentschura, Phys. Rev. B **564**, 225 (2003).

[43] V. A. Yerokhin and M. V. Shabaev, Phys. Rev. A **64**, 062507 (2001).

[44] V. A. Yerokhin, P. Indelicato and V. M. Shabaev, Phys. Rev. Lett. **91**, 073001 (2003).

[45] E.-O. Le Bigot et al., Phys. Rev. A **68**, 042101 (2003).

[46] U. D. Jentschura, P. Mohr and G. Soff, Phys. Rev. Lett. **82**, 53 (1999).

[47] S. Mallampalli and J. Sapirstein, Phys. Rev. A **57**, 1548 (1998).

[48] V. A. Yerokhin, P. Indelicato and V. M. Shabaev, Phys. Rev. A **71**, 040101 (2005).

[49] U. D. Jentschura, P. Mohr and G. Soff, Phys. Rev. A **63**, 042512 (2001).

[50] P. J. Mohr, Phys. Rev. Lett. **34**, 1050 (1975).

[51] K. Pachucki, Phys. Rev. Lett. **72**, 3154 (1994).

[52] U. D. Jentschura, J. Phys. A **36**, 229 (2003).

[53] S. G. Karshenboim, Sov. Phys. JETP **76**, 541 (1993).

[54] M. I. Eides and V. A. Shelyuto, Phys. Rev. A **52**, 954 (1995).

[55] U. D. Jentschura, A. Czarnecki, and K. Pachucki, Phys. Rev. A **72**, 062102 (2005).

[56] M. I. Eides et al., Phys. Rep. **342**, 63 (2001).

[57] U. D. Jentschura and M. Haas, Can. J. Phys. **85**, 531 (2007).

[58] V. A. Yerokhin, P. Indelicato, and V. M. Shabaev, Phys. Rev. A **71**, 040101(R) (2005).

[59] K. Pachucki and A. M. Moro, Phys. Rev. A **75**, 032521 (2007).

[60] Y. Yatsu et al., Nucl. Instr. Meth. A 564, 134 (2006).

[61] J. Sapirstein and D. R. Yennie, in *Quantum Electrodynamics*, Vol. 7 of *Advanced Series on Directions in High Energy Physics*, edited by T. Kinoshita (World Scientific, Singapore, 1990), pp. 560–672.